Characterization and Spatial Analysis of Official and Unofficial Caldera and Coronae Populations on Venus

Authored by:
Jess M. Woerner

Submitted to the Mount Holyoke College Department of Astronomy for the purpose of honors consideration

Advisor:
M. Darby Dyar

May 2024

Abstract

Venus is often considered Earth's evil twin due to their similarities in structure, but its surface conditions render it a volcanic hellscape. Through the mapping of previously defined populations of calderas and coronae on Venus using ArcGIS Pro, many features considered "caldera-like" and "coronae-like" were identified, prompting the creation of potential caldera and potential coronae catalogues. Heat maps were created to assess the spatial distribution of these features across the surface of Venus and it was found that 61% of the identified potential calderas were contained within or closely associated with the official caldera population, while 85% of the identified potential coronae were contained within or closely associated with the official coronae population. Further analysis of high-density feature clusters uncovered a significant presence of coronae with depressed topography as well as relationships between highly deformed terrain and coronae formation on the surface. A previously undocumented coronae cluster was identified in the Bereghinya Planitia quadrangle, outside of the distinct geologic settings in which coronae are most common. Upcoming missions to Venus will produce higher-resolution radar maps of the surface, allowing closer research of these findings.

TABLE OF CONTENTS

Acknowledgements

This thesis would not have been possible without the support and mentorship of Dr. Lauren Jozwiak of the Johns Hopkins University Applied Physics Laboratory in Laurel, Maryland. Thank you for taking a chance on me, and for your continued support and insight throughout this project.

I would like to thank my committee members: Dr. Darby Dyar, Dr. Thomas Burbine, and Dr. Claire Pless. Darby, you have been the best advisor I could have ever asked for. Thank you for your constant encouragement and feedback. I would not have discovered my love for planetary science without you, and you have changed my life for the better. Tom, you are one of the best professors I've had in my time at Mount Holyoke. Thank you for your humor and kindness. Claire, thank you for being there for me as both a mentor and a friend. I will always cherish our times in the rock room!

I would not have made it this far without my friends and loved ones. To Hayley, my partner in planetary science crimes, for your friendship and support. To Edith, my favorite goalie, for always making me laugh. To Amelia, Rose, Emily, and Gabby, for always being there for me when I needed it the most. To Mars and Micah, for always making me smile. To Eli, my brilliant partner. You are the smartest person I've ever known. Thank you for your love over these last four years. Finally, to my mom, for being a role model and my biggest supporter. Thank you for all the Take Your Child to Work days and encouraging my love for science. Thank you for the unconditional love and support. You are the strongest person I know, and I wouldn't be here without you.

Finally, I would like to thank the Mount Holyoke Astronomy and Geology departments for welcoming me with open arms and teaching me everything I needed to know and more, with a special thanks to Stevie Dunn and Al Werner for helping me realize how much I love geology! These departments have been my home for the last three years, and I will miss it dearly.

List of Figures

List of Tables

1. Introduction

Venus, the second closest planet to our Sun, is Earth's evil twin from hell.

This is not an exaggeration. Venus has a mass of $4.87 * 10^{24}$ kilograms (kg) and a mean radius of 6,051.8 kilometers (km), which is 81.5% of the mass of Earth and 95% of the radius of Earth, respectively (Sheehan & Limaye, 2022). Despite these similarities in size, the two planets have completely opposite conditions. Venus has an atmosphere composed of roughly 97% carbon dioxide (CO_2). Due to its proximity to the Sun, Venus receives twice as much solar radiation as Earth (Cattermole, 1994). This heats the surface, and the energy is re-emitted in the form of thermal energy at infrared wavelengths. The opaque nature of the Venusian atmosphere prevents the thermal energy from escaping into space, creating a runaway greenhouse effect (Hunt & Moore, 1982). As a result, the average surface temperature on Venus is a scorching 737 Kelvin (K), equivalent to 464 degrees Celsius (°C) (Sheehan & Limaye, 2022). Venus is dominated by volcanism and its surface has been extensively altered by volcanic and tectonic processes. However, the planet lacks true plate tectonics, like those observed on Earth (Hansen et al., 1997). Impact crater size-frequency distributions have been used to estimate the relative surface age of Venus as between 300 and 500 million years (Myr),

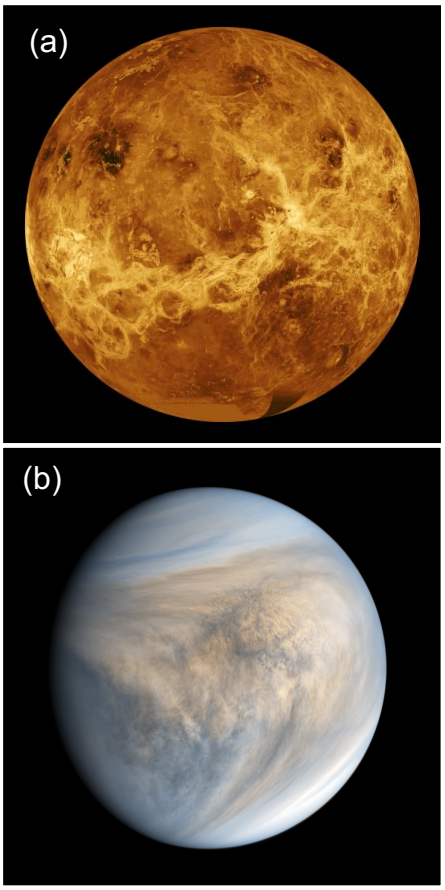

Figure 1. The planet Venus. (a) Simulated color image of the surface of Venus, centered at 180 °E longitude (NASA/JPL). (b) Ultraviolet image showing cloud structure in the Venusian atmosphere (JAXA).

with some studies giving age estimates of at least 750 Myr (Basilevsky et al., 1997). A geologically young surface may indicate relatively recent or ongoing volcanic activity on Venus, but this has never been directly observed.

In March 2023, it was announced that a volcanic vent that changed shape in the 8-month interval between *Magellan* imaging cycles had been identified, accompanied by a potential lava flow downhill from the vent (Herrick & Hensley, 2023). This does not necessarily confirm the presence of active volcanism on Venus because it is not a direct observation of a volcanic eruption, but it is extremely promising. Additionally, two new missions to Venus were recently selected by the National Aeronautics and Space Administration (NASA): VERITAS (Venus Emissivity, Radio Science, InSAR, Topography, and Spectroscopy) and DAVINCI (Deep Atmosphere Venus Investigation of Noble gases, Chemistry, and Imaging). The VERITAS orbiter will create a new, higher-resolution global map of the surface, look for thermal and chemical indicators of volcanic activity, and investigate potential surface changes. The DAVINCI probe and flyby mission will study the composition and physical properties of the atmosphere and attempt to land a probe on the surface that will collect composition and topography data as it travels through the atmosphere. The European Space Agency (ESA) also has an upcoming orbital mission to Venus, EnVision. NASA is providing the Synthetic Aperture Radar mapping instrument for EnVision which, combined with radio instrumentation and a suite of spectrometry instruments, will use surface and atmospheric measurements to characterize volcanic activity on Venus. As of October 2023, VERITAS and EnVision are projected to launch no earlier than the year 2031, while DAVINCI will launch in June 2029 (Widemann et al., 2023). The data returned by VERITAS, DAVINCI, and EnVision will hopefully answer many of our lingering questions about Venus.

The purpose of this thesis is twofold: to build on previous schema used to characterize volcanic features on the surface of Venus with a specific focus on coronae and calderas, and to construct a global map of coronae and calderas to investigate their spatial relationship. A caldera is a circular volcanic depression that forms after the emptying of an underlying magma chamber during a major eruption (Crumpler et al., 1997). Coronae are a type of volcanic feature first identified on Venus that tend to have raised topography, characterized by a surrounding annulus of concentric fractures and the presence of radially oriented fractures in their interior. It is believed that coronae form through an initial stage of volcanic uplift, typically accompanied by tectonic deformation and continued volcanism, followed by gravitational relaxation and a minor reduction in topography. Most coronae retain their raised topography, while some coronae, around one-third of the total population, present with depressed interiors (Stofan et al., 1997). The prevalence of coronae with depressed topography has led to some coronae being previously categorized as calderas, and some calderas being previously categorized as coronae. There are also several large volcanoes on Venus that are classified as having caldera- and/or corona-like features that are not included in official caldera or coronae populations. This thesis aims to identify potential calderas and coronae, map these features alongside the official caldera and coronae populations, and identify any spatial relationships or significant feature clusters on the surface of Venus.

2. Background

2.1. Venusian Geology

This section explores the geological characteristics and timing of geologic activity on Venus, specifically focusing on its volcanic history. The main focus of this study is the characteristics and formation of calderas and coronae on Venus, so these features are discussed in-depth.

2.1.1. Geological Evolution of Venus

The impact crater record on Venus is unique in that 84% of its craters are in pristine condition (Strom et al., 1994). This, coupled with the relatively low estimated surface age of 300 to 500 Myr, indicates large-scale resurfacing events have erased much of the surficial geological record on Venus. Venus, along with the rest of the Solar System, formed roughly 4.6 billion years ago, meaning that roughly 90% of its surface history has been erased by planetary resurfacing (Basilevsky et al., 1997). Two different models of resurfacing have been proposed: non-catastrophic equilibrium resurfacing (Phillips et al., 1992) and catastrophic global resurfacing (Schaber et al., 1992). Extensive resurfacing of the surface may have also contributed to the runaway greenhouse effect seen in the Venusian atmosphere due to repeated volcanic eruptions.

There are two main theories of geological evolution on Venus: directional and non-directional. The directional evolution hypothesis is based on extensive photogeological analysis of 36 randomly selected areas on Venus (Basilevsky & Head, 1995a,b). Subsequent analysis of larger regions produced a global stratigraphic model in which different tectonic processes dominated the surface at different times (Basilevsky & Head, 1995b). The oldest geological unit on Venus is the Fortuna Group, dominated by highly deformed tessera terrain (Tt) that covers

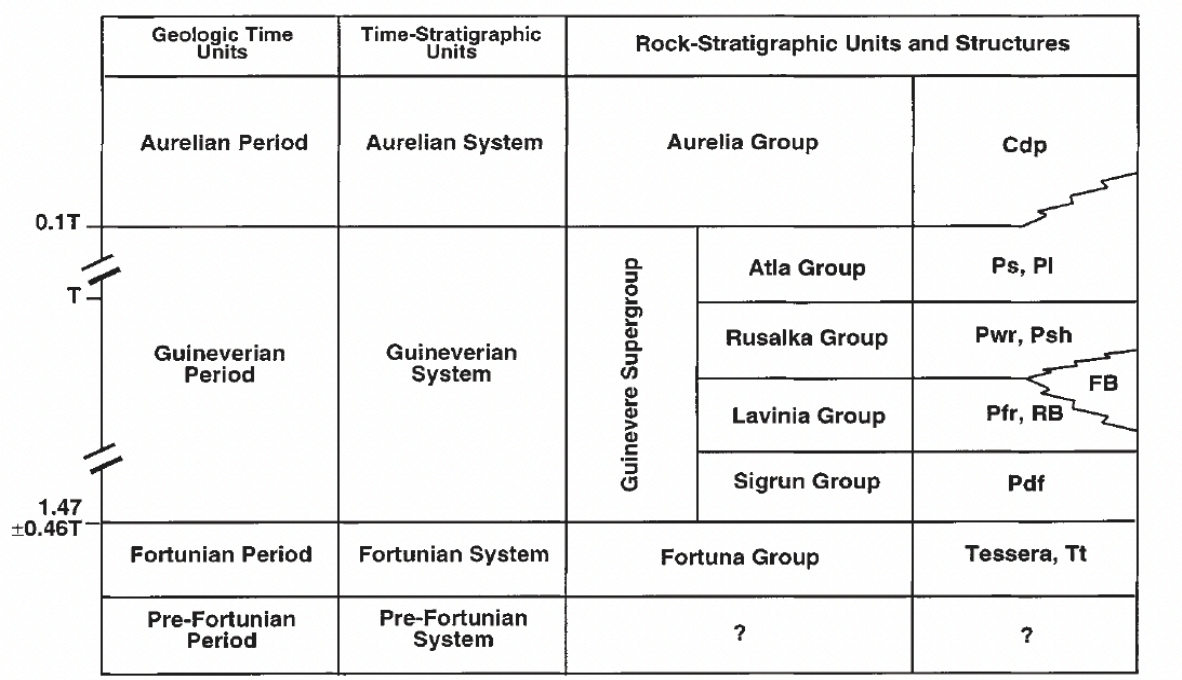

Figure 2. Directional theory of planetary evolution on Venus. Venus rock-stratigraphic units and their correlation with observed geologic time units. T represents the average age of the surface. Adapted from Basilevsky and Head, 1998.

about 8% of the surface. The relative age of the tessera terrain is supported by the observation that all other stratigraphic units on the surface either overlie or embay the terrain. Tessera morphology is dominated by intersecting tectonic ridge and groove systems, in which the deformation does not extend into the surrounding plains (Basilevsky & Head, 1995b). Additionally, tessera terrain is characterized by high topography and radar brightness (Basilevsky & Head, 1998).

The next stratigraphic unit, the Guinevere Supergroup, is comprised of four plains-forming material units. These units are distinguished by non-uniform episodes of tectonic deformation. The first unit of the Guinevere Supergroup is the Sigrun Group, which is characterized by densely fractured plains material (Pdf) that covers roughly 3% of the planetary surface. These plains may have been emplaced by mafic lava floods (Basilevsky & Head,

1995b). The next unit of the Guinevere Supergroup is the Lavinia Group, which consists of fractured and ridged plains material (Pfr) that, when clustered, form ridge belts (RB). This unit also covers 3% of the surface. Undeformed Lavinia Group materials are similar in appearance to the overlying plains, again indicating emplacement from mafic lava floods (Basilevsky & Head, 1995b). The next unit of the Guinevere Supergroup, the Rusalka Group, is the most abundant unit on Venus, covering 70 to 75% of the surface. (Basilevsky & Head, 1998). It consists of both shield plains material (Psh) and wrinkle ridge plains material (Pwr), the latter of which comprises 60 to 65% of Venus. (Basilevsky & Head, 1995b). The shield plains material is radar dark and contains small shields, likely of volcanic origin. The wrinkle ridged plains material shows evidence of deformation after its emplacement and tend to be radar dark but may also appear with mottled or radar bright terrain. Some regions of Venus contain fracture belts (FB) that cut through Lavinia Group terrain and are embayed by Rusalka Group materials. The materials within these fracture belts tend to be heavily deformed (Basilevsky & Head, 1995b). The last unit of the Guinevere Supergroup, the Atla Group, is characterized by undeformed lobate plains material (Pl) and smooth plains material (Ps) that covers 10 to 15% of the surface. These features are superposed by older wrinkle ridge plains materials. Atla Group materials tend to be associated with rift zones (Basilevsky & Head, 1995b). Finally, the youngest stratigraphic unit on Venus is the Aurelia Group, which consists of the radar-dark parabolas of younger impact craters (Cdp) superposed on all older units (Basilevsky & Head, 1998).

Ivanov & Head (2015) expands on this model by defining three global regimes of geological activity on the surface. The global tectonic regime comes first, defined by an earlier phrase of contraction and a later phase of extension during the Fortunian to mid-Guineverian epochs. The dominant stratigraphic units were tessera, lineated plains, ridged plains, and

ridge/groove belts. The global tectonic regime established a global topographic pattern and plateau-like highs and regional basins on the surface. The next epoch, the global volcanic regime, was dominated by contractional strain from wrinkle ridges and dike-related graben during the mid- to end of the Guineverian period. Structures emplaced during this era include shield plains and upper/lower regional plains. Additionally, the global topography was readjusted during this time, likely due to volcanic infilling of basins. The last regime, the network rifting-volcanism regime, occurred during the Atlian Period of the Guinevere Supergroup. This epoch was dominated by extensional strain at rift zones and coronae in the Beta-Atla-Themis region on Venus. The dominant structures emplaced during this regime included lobate plains, and rifted rises continued to develop on the surface during this time (Ivanov & Head, 2015).

The second theory of geological evolution on Venus is the non-directional hypothesis, first introduced in Guest & Stofan (1999). This theory argues that there is evidence that features such as coronae, rifts, wrinkle ridges, and flow fields have each formed throughout the history of Venus, with some processes occurring multiple times. Thus, Venus may have evolved in a similar manner as Earth, in which an overall non-directional emplacement history was modified by some directional events (i.e., impact cratering and highland plateau formation) (Guest & Stofan, 1999). There is strong evidence to support both the directional and non-directional hypotheses, but the directional hypothesis appears to dominate the field of Venus study.

2.1.2. Summary of Volcanism on Venus

Volcanism is the dominant geological process on the surface of Venus. Recent analysis of *Magellan* imagery has shown that Venus has nearly 85,000 volcanic edifices, 99% of which are over 5 km in diameter (Hahn & Byrne, 2023). This estimate is much larger than previous surveys

of the Venus volcanic population. For the purposes of this thesis, original catalogues of volcanoes and volcanic centers on Venus, primarily Crumpler et al. (1997) will be referenced.

Crumpler et al. (1997) identifies two main classes of volcanic features on Venus: extrusive and intrusive structures. The extrusive category can be further split into vents and fields. Vents often originate from a singular edifice and include the following features: large volcanoes (diameter ≥ 100 km), intermediate volcanoes (D < 100 km) and calderas. The intermediate volcano category includes radial flows, steep-sided domes, and fluted domes. Fields of shield volcanoes encompass most of the small volcanoes on Venus (diameter < 20 km) and are the single most common type of volcanic center on the surface (Crumpler et al., 1997). Extrusive features form through the accumulation and emplacement of erupted materials. Intrusive volcanic structures include coronae, arachnoids, and stellate fracture centers. These features form due to the emplacement of magma chambers below the surface.

2.1.3. Calderas and Coronae: Characteristics and Classification

Calderas (Figure 3a) are volcanic depressions that form after the collapse of a magma chamber associated with an explosive or rapid eruption (Crumpler et al., 1997). They have circular to elongate shapes and are typically not associated with a well-defined volcanic edifice. Calderas can be identified by concentric enveloping fractures and a smooth, radar-dark central region. They are distinguished from impact craters by the absence of a hummocky raised rim and speckled ejecta pattern. A specific subtype of caldera, called a patera (paterae), is characterized by scalloped margins and a flat interior floor with exterior radial lava flows. Calderas can have a diameter of up to 200 km but are most abundant in the range of 40 to 80 km diameter (Head et

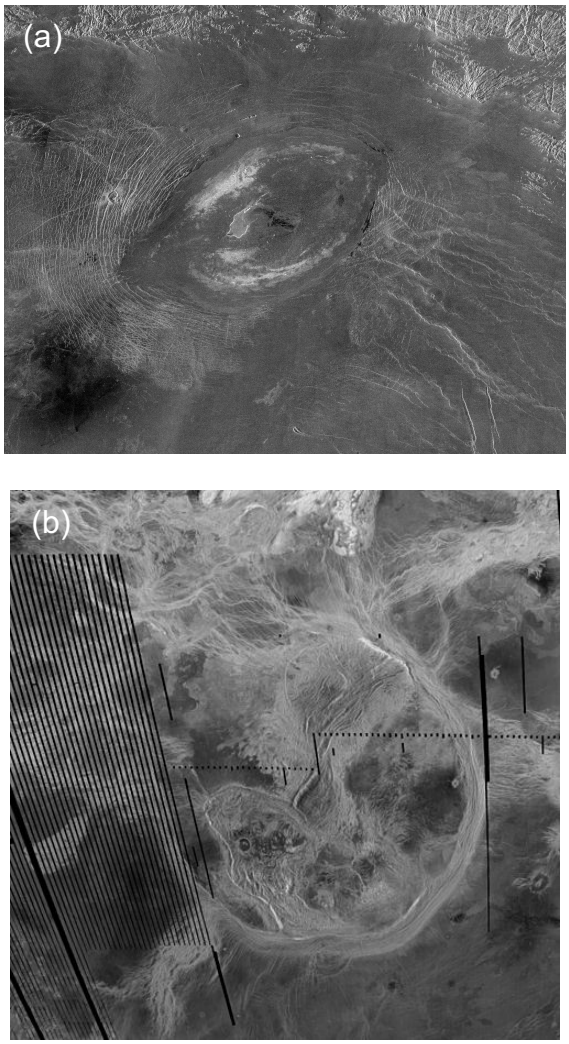

Figure 3. Calderas and Coronae on Venus. (a) Radar image of Sacajawea Patera (64.5 °N/-23.4 °W), a large elongate caldera. Diameter: 233 km. (NASA/JPL). (b) Radar image of Artemis Corona (-35 °S/135 °E), the largest corona on Venus. Diameter: 2,600 km. (NASA/JPL)

al., 1992). A total of 96 calderas, all greater than 20 km in diameter, have been identified by Crumpler et al. (1997).

Coronae (Figure 3b) are intrusive features, most of which exhibit raised topography, characterized by an annulus of concentric fractures and the presence of radially oriented fractures in their interiors. Coronae form through an initial stage of volcanic uplift accompanied by tectonic deformation and continued volcanism, followed by gravitational relaxation and a minor reduction in topography. The volcanic uplift is often caused by a diapir, a type of volcanic intrusion in which a more mobile material is pushed into a brittle overlying rock layer. While most coronae retain a positive topographic signature, about one-third of the total coronae population have interior depressions (Stofan et al., 1997). Most coronae have diameters between 200 and 250 km, but there are some with higher diameters above 600 km and a few occurring upwards of 800 km (Head et al., 1992). A total of 341 coronae have been named and approved by the United States Geological Survey (USGS)/International Astronomical

Union (IAU) Gazetteer of Planetary Nomenclature[1]. It should also be noted that coronae have only been observed on Venus.

Some calderas (Sappho, Sacajawea, and Colette Paterae) were previously included in the coronae population described in Stofan et al. (1992) despite being officially recognized as paterae in the USGS/IAU Gazetteer of Planetary Nomenclature. Additionally, some coronae (Nintu, Holla, Emegelji, Erigone, Pachamama, Derceto, Cailleach, Sarpanitum, and Mykh-Imi Coronae) were included in the Crumpler et al. (1997) caldera population. Stofan et al. (1997) hypothesizes that, given the similarities between large-scale calderas on Venus and some coronae, late-stage collapse or down-sagging may be an important process in corona evolution. These discrepancies in caldera and corona populations, as well as the similarities between the two features, were the initial inspiration for this thesis.

2.2. Previous Exploration of Venus

Beginning in the 1960s, Venus has been visited by six missions (including *Magellan*) from the United States and fifteen missions from the Soviet Union (Tanaka et al., 1993). Additional Earth-based radar observations have been made at the Arecibo Observatory in Puerto Rico, the Goldstone Deep Space Communications Complex in California, and the Massachusetts Institute of Technology (MIT) Haystack Observatory in Massachusetts (Ford, 1993).

[1] https://planetarynames.wr.usgs.gov/SearchResults?Target=15_Venus&Feature%20Type=8_Corona,%20coronae.

2.2.1. Orbiters, Probes, and Landers

This section serves as a short summary of previous missions to Venus, sent by both the United States (Table 1) and the Soviet Union (Table 2). Specific mission details were adapted from Siddiqi (2018).

Table 1. Successful United States Missions to Venus, Pre-*Magellan*.

Mission Name	Launch Date	Mission Summary
Mariner 2	August 27, 1962	**First successful flyby of another planet on December 14, 1962.** Took basic measurements of temperature distribution across the surface and collected atmospheric data.
Mariner 5	June 14, 1967	Successful flyby on October 19, 1967. Collected data on surface temperature and pressure. Discovered that the planet's ionosphere produces a bow shock that deflects solar wind around the planet, rather than an intrinsic magnetic field.
Mariner 10	November 3, 1973	Successful flyby on February 5, 1974. The spacecraft approached Venus to perform a gravity-assist maneuver to the planet Mercury, the main target of the mission. *Mariner 10* returned 4,165 images of Venus.
Pioneer Venus 1 (PV Orbiter)	May 20, 1978	**Entered orbit on December 4, 1978, as the first American spacecraft to orbit Venus**. Topographic mapping of the surface between 73 °N and 63 °S at a 75 km resolution was compiled using radar data acquired by the orbiter. Maxwell Montes was identified as the highest point on Venus. Confirmed the lack of a magnetic field and documented ionosphere-solar wind interactions that had been previously identified.
Pioneer Venus 2 (PV Multiprobe)	August 8, 1978	Atmospheric entry on December 9, 1978. Spacecraft consisted of a main bus, one Large Probe, and three identical Small Probes – all of which collected data as they travelled through the atmosphere. Transmissions from the Large Probe and one of the Small Probes ceased on impact. The two remaining Small Probes survived surface impact, one of which continued to transmit data for 67 minutes post-impact. Data from the probes indicated a lack of convection between 10 and 50 km above the surface within the atmosphere. Additionally, temperature data collected by all four probes showed little variation despite the differences in their entry sites.

Table 2. Successful Soviet Union Missions to Venus, Pre-*Magellan*.

Mission Name	Launch Date	Mission Summary
Venera 4	June 12, 1967	Successful atmospheric entry on October 18, 1967. Spacecraft was not intended to survive on the surface but managed to return data on surface temperature and pressure as well as atmospheric composition.
Venera 5	January 5, 1969	Atmospheric entry for Venera 5 on May 16, 1969. Atmospheric entry for Venera 6 on May 17, 1969. Identical spacecraft launched five days apart. Landers designed to survive a maximum pressure of 25 atmospheres and a maximum temperature of 320 °C based on data from Venera 4. Measured a surface temperature of 530 °C and pressure of 140 atmospheres.
Venera 6	January 10, 1969	
Venera 7	August 17, 1970	**Landed on surface on December 15, 1970, as the first soft landing on another planet.** Spacecraft rolled upon landing, so data return was limited. Despite this, the lander recorded data for 22 minutes and 58 seconds after impact, which was the first data transmitted from another planet's surface. The spacecraft was designed to survive a maximum temperature of 540 °C and pressures of 150-180 atmospheres.
Venera 8	March 17, 1972	**First successful landing on another planet on July 22, 1972.** Spacecraft continued to transmit data for 50 minutes and 11 seconds after impact. Lander was designed to survive a maximum temperature of 493 °C and pressure of 105 atmospheres. The temperature at the landing site was 470 +/- 8 °C while the pressure at the landing site was 90 +/- 1.5 atmospheres. Wind velocity below 10 km altitude was recorded as less than 1 km/second. Potassium, uranium, and thorium (naturally occurring radioactive elements) identified in preliminary compositional data of surface collected by gamma-ray spectrometer.
Venera 9	June 8, 1975	Venera 9, **the first orbiter sent to Venus**, entered orbit on October 20, 1975, and its lander was deployed on October 22, 1975. Venera 10 entered orbit on October 23, 1975, and its lander was deployed on October 25, 1975. **Venera 9 collected the first images from the surface of another planet**: one of the two covers on the camera failed to release so a 180° panorama was produced rather than the intended 360° panorama. Image showed flat rocks on the surface near the lander. Venera 10 was also only able to produce a 180° panorama, but these photos were never released. Gamma-ray spectrometer and radiation densitometer onboard Venera 10 indicated a basalt-like surface composition, suggesting volcanic origin.
Venera 10	June 14, 1975	

Venera 11	September 9, 1978	Venera 11 landed on December 25, 1978. Venera 12 landed on December 21, 1978. Both landers experienced multiple instrument failures, particularly the soil sample collection/analysis and camera deployment. Venera 11 was able to collect soil but the chemical and physical analysis was unsuccessful. Both landers continued to transmit data for over an hour post-landing.
Venera 12	September 14, 1978	
Venera 13	October 30, 1981	Venera 13 landed on March 1, 1982. Venera 14 landed on March 5, 1982. Venera 13 produced the **first recording of sounds from another planet** and the **first color images of the surface of Venus.** The images showed a field of orange-brown angular rocks and loose soil. Soil analysis was successful and indicated high potassium content, similar to terrestrial leucitic basalt. The temperature and pressure recorded at the Venera 14 landing site were higher than that of the Venera 13 landing site.
Venera 14	November 4, 1981	
Venera 15	June 2, 1983	Venera 15 entered orbit October 10, 1983. Venera 16 entered orbit October 11, 1983. Both orbiters remained operational until July 1984. The mission was designed to expand on observations made by the Pioneer Venus Orbiter and produced a map of the northern hemisphere at a resolution of 1-2 km using synthetic aperture radar (SAR).
Venera 16	June 7, 1983	
Vega 1	December 15, 1984	Vega 1 landed on June 11, 1985. Vega 2 landed on June 15, 1985. Both landers deployed atmospheric probes during entry that operated for two days. The remaining spacecraft post-lander deployment were flown past Halley's Comet. The soil analysis on Vega 1 failed but its mass spectrometer returned some data. The soil analysis on Vega 2 was successful, identifying an anorthosite-troctolite rock (rare on Earth, but present in lunar highlands). The mass spectrometer onboard Vega 2 did not return any data. Neither atmospheric balloon detected lightning.
Vega 2	December 21, 1984	

2.2.2. Ground-Based Observations

Ground-based observations of Venus started in the 1960s using radio telescopes at the Arecibo Observatory in Arecibo, Puerto Rico; the Goldstone Deep Space Communications Complex in Goldstone, California; and the Massachusetts Institute of Technology (MIT) Haystack Observatory in Westford, Massachusetts (Ford, 1993). Radar coverage of these

telescopes was extremely limited, thus only 40% of the planet was mapped using their data (Tanaka et al., 1993). Most knowledge of Venus has come from subsequent synthetic-aperture radar images.

2.3. *Magellan*

2.3.1. Mission Objective

The *Magellan* spacecraft was launched by the National Aeronautics and Space Administration (NASA) from the Kennedy Space Center in Cape Canaveral, Florida onboard Space Shuttle Atlantis on May 4, 1989 (Ford, 1993). The shuttle crew deployed *Magellan* one day later and the spacecraft travelled in a trans-Venus interplanetary trajectory, reaching Venus after a 15 month-long journey on August 10, 1990 (Saunders et al., 1992). The first mapping cycle of the mission began on September 15, 1990. The *Magellan* mission had four scientific objectives: (1) to provide a global characterization of landforms and tectonic features; (2) to distinguish and understand impact processes; (3) to define and explain erosion, deposition, and chemical processes; and (4) to model the interior density distribution (Ford, 1993).

2.3.2. Instrumentation

Magellan was designed as a low-cost, high-performance spacecraft. It was built using spare components from previous missions, including the *Galileo* orbiter, the Mariner 9 orbiter, and the interstellar *Voyager* probes (Young, 1990). The main scientific instrument onboard *Magellan* is a radar system composed of multiple antennae that acquires data in three different modes: synthetic aperture radar (SAR), altimetry, and radiometry (Tanaka et al., 1993). Data were obtained using the burst-mode method, where the sensor acquires SAR, altimetry, and

radiometry data in sequential batches multiple times per second (Ford, 1993). A high-gain antenna (HGA) controls SAR and radiometer operations, while the altimeter antenna (ATLA) mounted aside the HGA controls altimetry measurements. SAR produces radar images of the surface, altimetry measures the height of surface features, and radiometry measures thermal emissions from the planet (Young, 1990).

Magellan's SAR operates at a 12.6 cm wavelength, which penetrates the opaque atmosphere and allows the radar return echoes to distinguish small-scale differences in surface roughness. (Ford, 1993). SAR image quality is impacted by several factors: spatial resolution, incidence angle, signal-to-noise ratio, the number of "looks", and amplitude resolution. The incidence angle is the angle between the incident radar energy that strikes the planetary surface and the line perpendicular to the surface at this point (Tanaka et al., 1993).

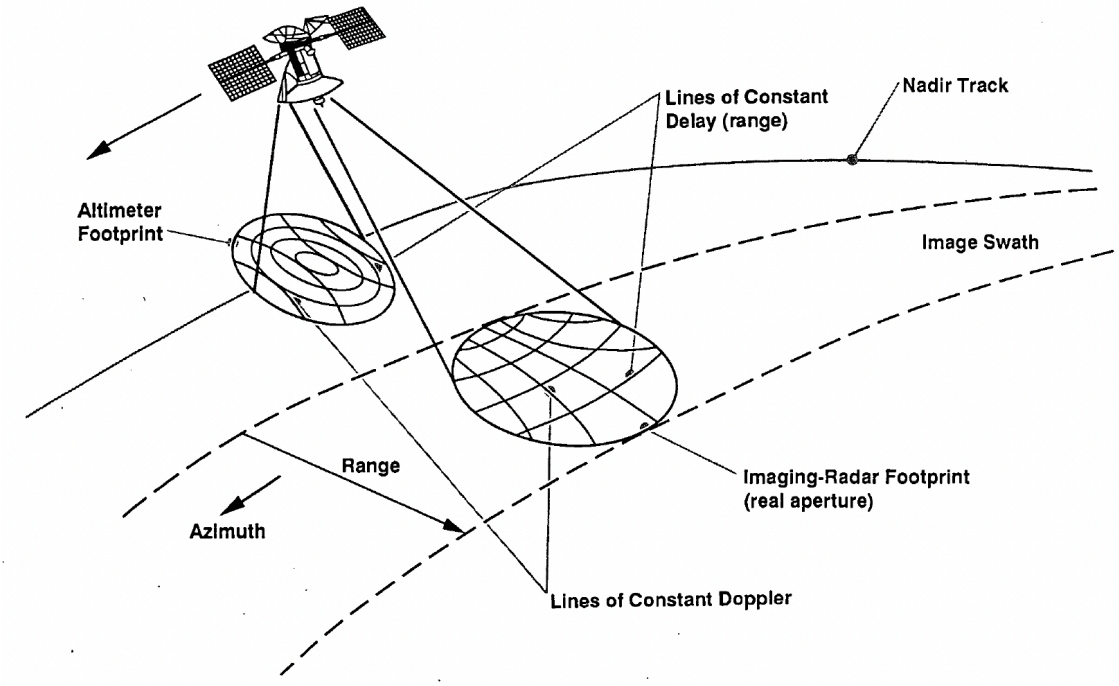

Figure 4. Diagram showing the viewing geometry of *Magellan* in its data collecting mode. Adapted from Ford et al. (1993).

The altimeter measures the distance between the spacecraft and the planetary surface which, combined with the spacecraft's position relative to the center of Venus, produces a topographic map of the surface (Ford, 1993). The radiometer indirectly measures radio emissivity of the planet's surface at the same 12.6 cm wavelength used by the SAR, which produces thermal radiation data. Thermal radiation data of an object with a known physical temperature are collected with the purpose of estimating the emissivity of said object. The emissivity is also impacted by the degree of surface roughness (Tanaka et al, 1993).

2.3.3. Mission Timeline and Mapping Cycles

Magellan completed six mapping cycles over the course of four years. Each mapping cycle lasted 243 days, the time it takes for Venus to complete one rotation on its axis under the spacecraft (Saunders et al., 1992). The first mapping cycle began on September 15, 1990, with the goal of creating a left-looking map of 70% of the surface at a minimum resolution of 1 km per pixel. Cycle 1 ended on May 15, 1991, and produced a left-looking map of 83.7% of the surface at a resolution of 101 to 250 m per pixel (Ford & Plaut, 1993). See Section 2.3.4. for an explanation of how "left-looking" and "right-looking" radar data is produced.

Cycle 2 began immediately after the conclusion of Cycle 1 on May 15, 1991. The goal of Cycle 2 was to fill in any image gaps from Cycle 1 and to begin imaging the south pole region of Venus. The spacecraft was reoriented to enable right-looking data collection. This cycle ended on January 14, 1992, after collecting right-looking data for 54.5% of the surface. Cumulatively, 96% of the surface had now been mapped. (Ford & Plaut, 1993).

Cycle 3 began on January 15, 1992, with the goal of collecting stereo image data. Stereo imaging would allow three-dimensional renderings of the surface to be created. Cycle 3 ended on

September 13, 1992, after stereo images had been collected for 21.3% of the surface and an additional 2% of the planet was covered at the original left-looking configuration from Cycle 1. Overall, 98% of the surface had been imaged and the radar mapping portion of the mission was finished (Ford & Plaut, 1993).

Cycle 4 began on September 14, 1992, and marked the start of *Magellan*'s gravity observations. Gravity data was acquired by pointing the spacecraft's high-gain antenna toward Earth and record changes in the Doppler shift of the radio signal. A change in Doppler shift indicated that the spacecraft was passing over areas of higher gravitation, which would cause its velocity to increase. Cycle 4 ended on May 23, 1993 (Ford & Plaut, 1993).

Cycle 5 started with an aerobraking maneuver designed to circularize the orbit of the spacecraft, which allowed for higher-resolution gravity data to be collected. The aerobraking phase started on May 24, 1993, and ended August 2, 1993 (Lyons et al., 1995). Actual gravity measurements began on August 3, 1993, and ended on August 29, 1994. By this time, high-resolution gravimetric data had been collected for around 95% of Venus.[2]

Cycle 6 extended previous gravimetric studies, but its main focus was the windmill experiment, which began on September 6, 1994. *Magellan*'s orbit was lowered into the atmosphere and its solar panels were tilted, which put a torque on the spacecraft due to atmospheric drag. To counter the torque, the thrusters were fired to prevent the spacecraft from spinning. Measurements of the corrections needed to offset the torque were recorded to help provide an understanding of the impact of upper-atmospheric forces. The windmill experiment ended on September 14, 1994. *Magellan* began its final orbital maneuver to prepare for

---

[2] https://nssdc.gsfc.nasa.gov/planetary/mgncycles.html.

atmospheric entry on October 11, 1994. Radio signal was lost on October 12, 1994, and the spacecraft likely began its atmospheric entry shortly after, signaling the end of the mission.[2]

2.3.4. Radar Data Interpretation, Image Data Records, and Mosaicking

Magellan followed an elliptical, north-to-south orbit around Venus. When the SAR was pointed to the east relative to its orbit, it was producing "left-looking" data. "Right-looking" data was produced when the SAR was oriented to the west relative to its orbit. There are three variables that affect radar brightness in *Magellan* images: (1) topographic effects, (2) surface roughness, and (3) electrical properties. Terrain that slopes towards the sensor has a higher radar brightness than terrain that slopes away from the sensor. Additionally, rougher surfaces have higher backscatter than smooth surfaces, and high backscatter correlates with radar brightness. The inherent reflectivity properties of a surface also influence radar brightness. For example, a high dielectric constant increases radar backscatter. (Ford & Plaut, 1993).

A total of 4,225 usable SAR imaging orbits were obtained during first three mapping cycles, where the area covered by each orbit was 20 km wide and 17,000 km long. Raw SAR data was first processed into basic image data records (BIDRs). Each BIDR strip was accompanied by a corresponding altimeter/radiometer composite data record (ARCDR), which represented all of the data obtained in each orbit. From these two components, a full-resolution BIDR (F-BIDR) was produced as the primary image data product. Adjacent F-BIDRs were assembled into mosaicked image data records (MIDRs), the standard *Magellan* photographic image products. Mosaicking algorithms were developed to produce smoother boundaries between adjacent orbits in the final product. However, there is dark or bright banding in some mosaics that can be seen running parallel to orbital boundaries due to small differences in

antenna pointing, topographic mapping, or spacecraft navigation which resulted in slightly inaccurate radiometric factors being applied to the image during processing. Full-resolution mosaicked image data records (F-MIDRs) used the full resolution, 75 m per pixel, of their respective input F-BIDRs. F-MIDRs cover an area approximately 5° latitude by 5° longitude. Mosaics of larger areas can be created by compressing the resolution of input F-BIDRs. There are three levels of compressed MIDRs. A Compressed-Once Mosaicked Image Data Record (C1-MIDR) has a 225 m per pixel resolution and covers an area 15° latitude by 15° longitude. A Compressed-Twice Mosaicked Image Data Record (C2-MIDR) has a 675 m per pixel resolution and covers an area 45° latitude by 45° longitude. A Compressed-Thrice Mosaicked Image Data Record (C3-MIDR) has a 2,025 m per pixel resolution and covers an area 80° latitude x 120° longitude. C1-MIDRs are produced from Compressed-Once Basic Image Data Records (C1-BIDRs), while C2- and C3-MIDRs are produced by further compression of C1-MIDRs. After the mosaicking process is finished, the image products are contrast enhanced, annotated, and masked to allow the output of photographic data used in scientific analysis (Ford & Plaut, 1993).

Stereo radar images collected by *Magellan* were used to produce topography data for 20% of the surface by Herrick et al. (2012). The stereo-derived topography has a finer horizontal resolution of 1-2 km, compared to *Magellan*'s altimetry data which has a horizontal resolution of 10-20 km. Match points (points on different images depicting the same feature) were identified between the mosaicked stereo data and the 75 m/pixel surface map created using the *Magellan* F-BIDRs. The match points define parallax values and were converted to relative elevations based on the angle of the spacecraft's antenna. The stereo-derived elevations were combined with the *Magellan* altimetry data and filtered to determine absolute elevation (Herrick et al., 2012). The

stereo-derived topography covers Maxwell Montes, as well as areas in Eistla Regio, Tellus Regio, and Ovda Regio.

3. Methods

3.1. Database Creation

The official caldera population was adapted from Crumpler et al. (1997) (Table II, CDP6C1T2), while the official corona population was adapted from the USGS/IAU (United States Geological Survey/International Astronomical Union) Gazetteer of Planetary Nomenclature. Some of the calderas identified by Crumpler et al. (1997) were unnamed, so their coordinates were cross-referenced with the Gazetteer of Planetary Nomenclature to fill these gaps. This database includes 96 official calderas and 341 official coronae.

A population of potential calderas was curated from multiple sources. Some paterae (a subtype of caldera with scalloped edges) identified in the Gazetteer of Planetary Nomenclature were not included in the Crumpler et al. (1997) caldera population. Additionally, the Gazetteer of Planetary Nomenclature identified some coronae that had been previously classified as paterae. The morphological classification of multiple large volcanoes in the Crumpler et al. (1997) large volcano population (Table I, CDP6C1T1) also indicated caldera-like features. Thus, large volcanoes that were Class II (Caldera) and Class IV (Elongated Summit) were also included in the potential caldera population. Class IV volcanoes were included in this population since they often contain multiple caldera-like features (Crumpler et al., 1997). Finally, independent summit calderas were included: two summit calderas on Tepev Mons (Campbell & Rogers, 1994), one summit caldera on Maat Mons (Mouginis-Mark, 2016), and one summit caldera on Mielikki Mons (Stofan et al., 2016). Overall, 66 potential calderas were identified.

A population of potential coronae was also curated from features that had been previously classified as coronae by the Gazetteer of Planetary Nomenclature and Class IX (corona-like

interiors) large volcanoes (Crumpler et al., 1997, Table I, CDP6C1T1) that were not already included in the official coronae population. Additionally, any features labeled as Class IX large volcanoes that corresponded with a caldera or patera were excluded from the potential coronae population, instead included in the caldera populations. Overall, 13 potential coronae were identified.

The features in each category were further organized by geologic setting and feature topography. Four geologic setting classifications were created: volcanic – low, volcanic – high, tectonic – rift, and tectonic – wrinkle ridge. The geologic setting of a feature was determined based on its larger surrounding features. Volcanic – low features were all found in planitia/planitiae (low lava plains). Volcanic – high features were found in volcanic highlands and high lava plains, i.e., tessera/tesserae (heavily deformed terrain with high topography), terra/terrae (extensive highland land mass), regio/regiones (volcanic rises), and planum/plana (high lava plain or plateau). Tectonic – rift features were associated with rift valleys (fossa/fossae and linea/lineae) and rift chains (chasma/chasmata). Tectonic – wrinkle ridge features were all associated with dorsum/dorsae (ridges).

Feature topography profiles were first derived from Hamilton & Stofan (1995) and Martin et al. (2007). Hamilton & Stofan (1996) analyzed the geomorphology and evolution of Hecate Chasma, a rift belt extending northeast from Atla Regio to Asteria Regio over 8,000 km in length. Table 1 in Hamilton & Stofan (1996) provides a list of the coronae in Hecate Chasma and identifies various characteristics, including feature topography. Martin et al. (2007) discusses coronae in Parga Chasmata, a 10,000 km long rift belt extending southeast from Atla Regio to Themis Regio. Table 1 in Martin et al. (2007) also provides a list of the coronae in Parga Chasmata and identifies feature topographies, among other characteristics. These tables provided

a basis for initial topographic classifications in the database. Topography for features not included in Hamilton & Stofan (1996) or Martin et al. (2007) was determined using a C3-MIDR colorized topography map. For this database, nine topographic profiles were identified, adapted from the classification systems used in Stofan et al. (1997), Hamilton & Stofan (1996), and Martin et al. (2007): dome/rise; rimmed rise; plateau; rimmed plateau; depression; rimmed depression; rim only; outer rim, trough, inner rise; and no discernable signature.

3.2. Mapping in ArcGIS Pro

A global map of official calderas, potential calderas, official coronae, and potential coronae was created using a full-resolution (75 m/pixel) map of the surface of Venus produced from *Magellan* F-BIDRs in the mapping software ArcGIS Pro. Each category was represented by its own feature class. In ArcGIS Pro, a feature class is a collection of common features, each with the same spatial representation on the map and a shared set of attributes. In this case, the features

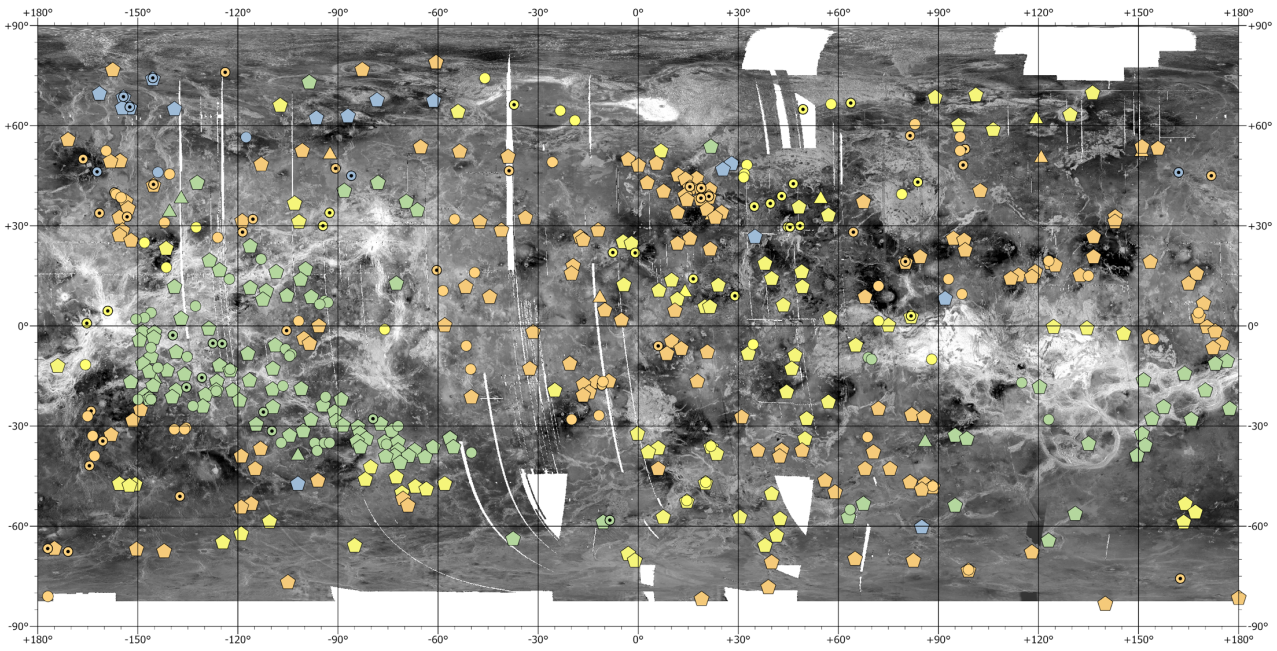

Figure 5. Global map of calderas, potential calderas, coronae, and potential coronae on Venus.

in each population were mapped as point features. Calderas were represented by circles, potential calderas were represented by circles with a center point, coronae were represented by pentagons, and potential coronae were represented by triangles.

The map also utilized unique value symbology for the point features. The unique value symbology was assigned based on the geologic setting attribute field. The orange and yellow points on the map represent volcanic – low and volcanic – high geologic settings, respectively. The green and blue points on the map represent tectonic – rift and tectonic – wrinkle ridge geologic settings, respectively. An analysis of the relationship between feature type, geologic setting, and feature topography will be presented in the Discussion section.

3.2.1. Attribute Tables

Each feature class had its own attribute table, organized in order from highest to lowest latitude. Attribute fields included in all four feature classes were: latitude, longitude, quadrangle, dimensions (km), name, surrounding feature, geologic setting, feature topography, and source. The feature names, quadrangles, and surrounding features for all four feature classes were determined using the Gazetteer of Planetary Nomenclature and USGS 1:5,000,000 scale nomenclature quadrangle maps. Feature topography was derived for all four feature classes using the schema described in Section 3.1.

The caldera attribute table was primarily adapted from Table II of Crumpler et al. (1997) (CDP6C1T2). This table contained the coordinates, dimensions, and some feature names. Nameless features had their coordinates cross-referenced with the Gazetteer of Planetary Nomenclature, allowing more of the features to be named in the final attribute table. Notes on the

appearance of each feature from Table II of Crumpler et al. (1997) (CDP6C1T2) were also included in the attribute table.

The potential caldera attribute table was adapted from multiple sources. The coordinates and dimensions of large volcanoes with caldera-like features (Class II and Class IX) were adapted from Table I of Crumpler et al. (1997) (CDP6C1T1). Nameless features were again cross-referenced with the Gazetteer of Planetary Nomenclature, allowing more features to be named in the final table. For paterae (calderas with scalloped edges), and coronae previously classified as paterae by the IAU, coordinates, dimensions, and feature names were derived from the Gazetteer of Planetary Nomenclature. Independent summit calderas were identified from Campbell & Rogers (1994), Mouginis-Mark (2016), and Stofan et al. (2016). The attributes of these features were also derived from the Gazetteer of Planetary Nomenclature.

The coronae attribute table was adapted from the list of named coronae in the USGS Gazetteer of Planetary Nomenclature. Attributes derived from this source were coordinates, dimensions, and feature names.

The potential coronae attribute table was also adapted from multiple sources. The coordinates and dimensions of large volcanoes with corona-like features (Class IX) were adapted from Table I of Crumpler et al. (1997) (CDP6C1T1). Nameless features were again cross-referenced with the Gazetteer of Planetary Nomenclature, allowing more features to be named in the final attribute table. For miscellaneous features previously classified as coronae by the IAU, coordinates, dimensions, and feature names were derived from the Gazetteer of Planetary Nomenclature.

3.2.2. Geoprocessing Techniques

Heat maps showing relative density across the surface of the planet were created using the heat map symbology method in ArcGIS Pro. This method was determined to be the most effective for visualizing the density of a large number of point features, especially since there were multiple areas on the map with overlapping points across multiple feature classes. Heat map symbology uses dynamic raster visualization to represent relative density, which is calculated using a kernel density geoprocessing algorithm. For each map created the radius (a set distance in screen unit points) was set to 25, the Dynamic rendering method was selected, and the rendering quality was set to Best to maximize image quality.

4. Results

Heat maps showing feature distribution and density were created for all four feature classes. Cooler colors (blue to purple) represent areas with a sparser density, and warmer colors (red to yellow) represent areas with a higher density.

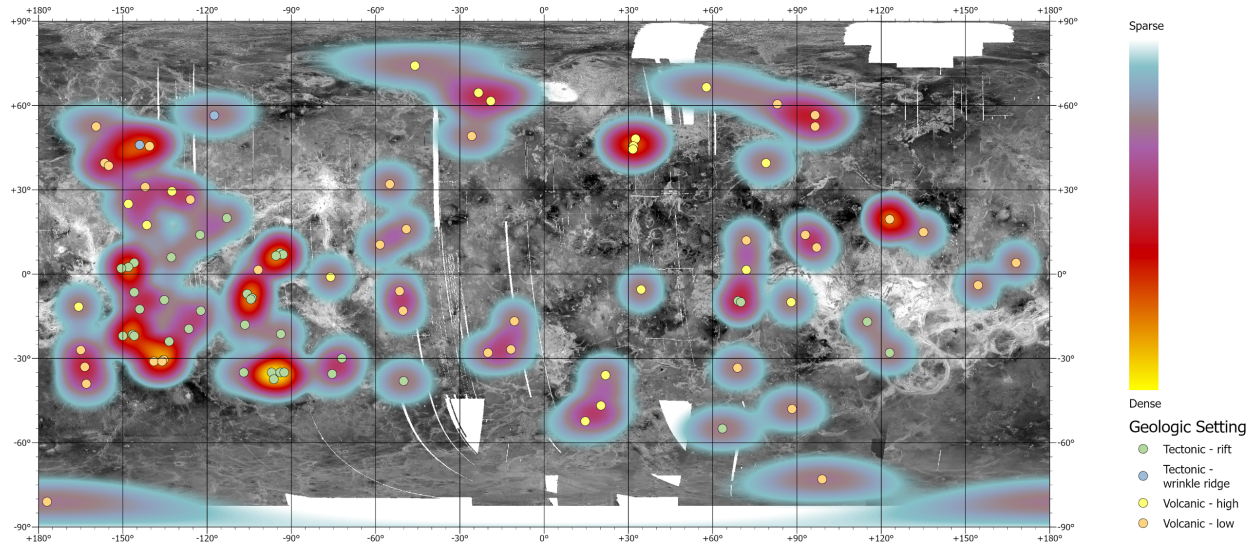

Figure 6. Heat map showing caldera density and distribution on the surface of Venus. Points show exact location of features based on coordinates.

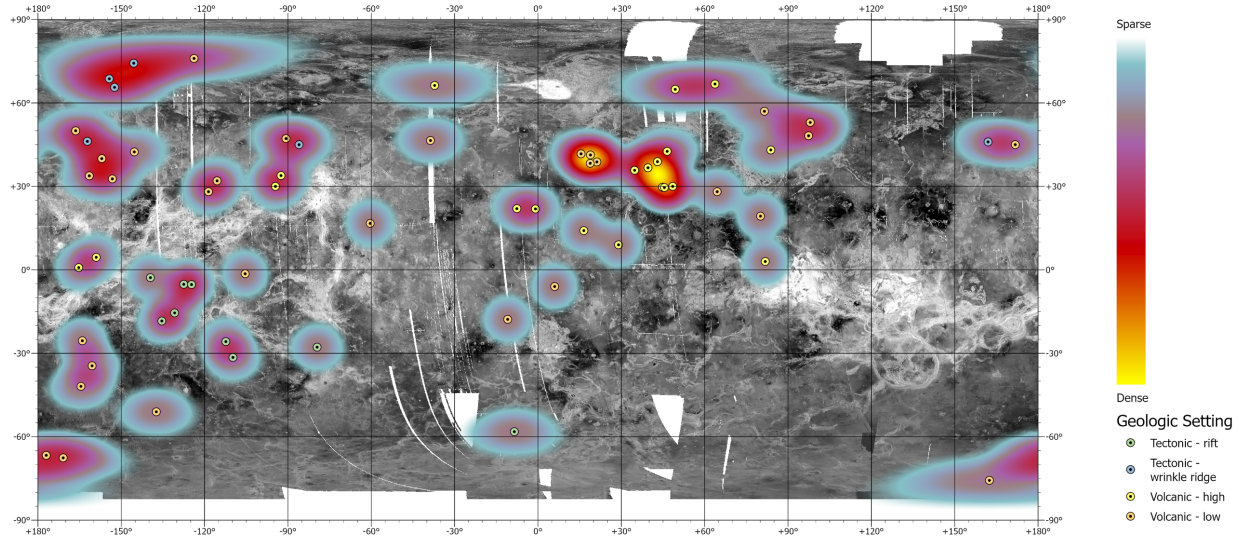

Figure 7. Heat map showing density and distribution of potential calderas on the surface of Venus. Points show exact location of features based on coordinates.

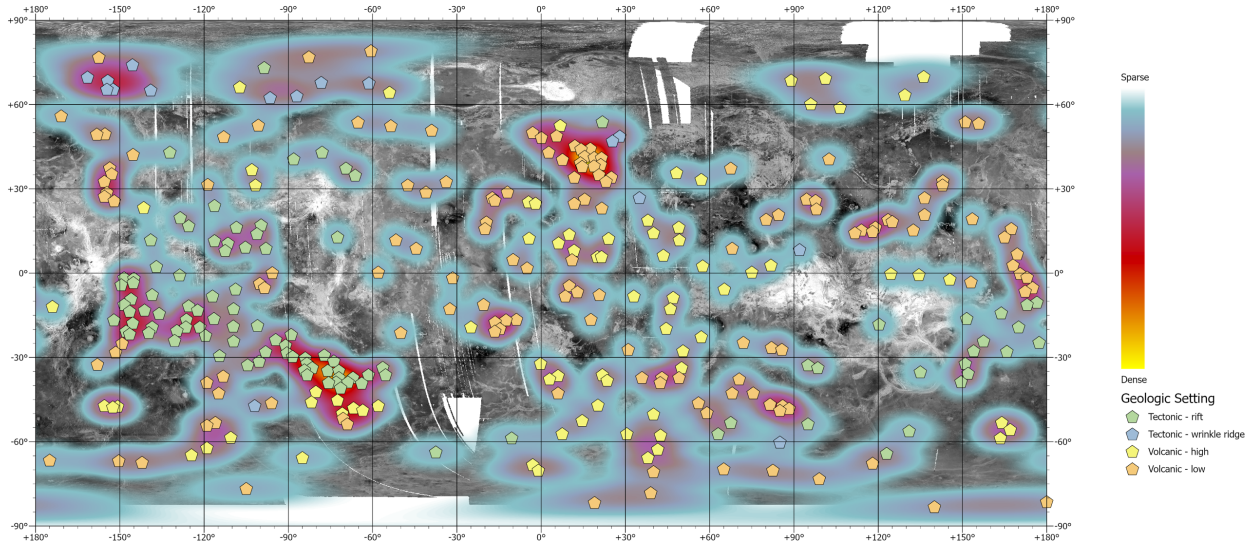

Figure 8. Heat map showing coronae density and distribution on the surface of Venus. Points show exact location of features based on coordinates.

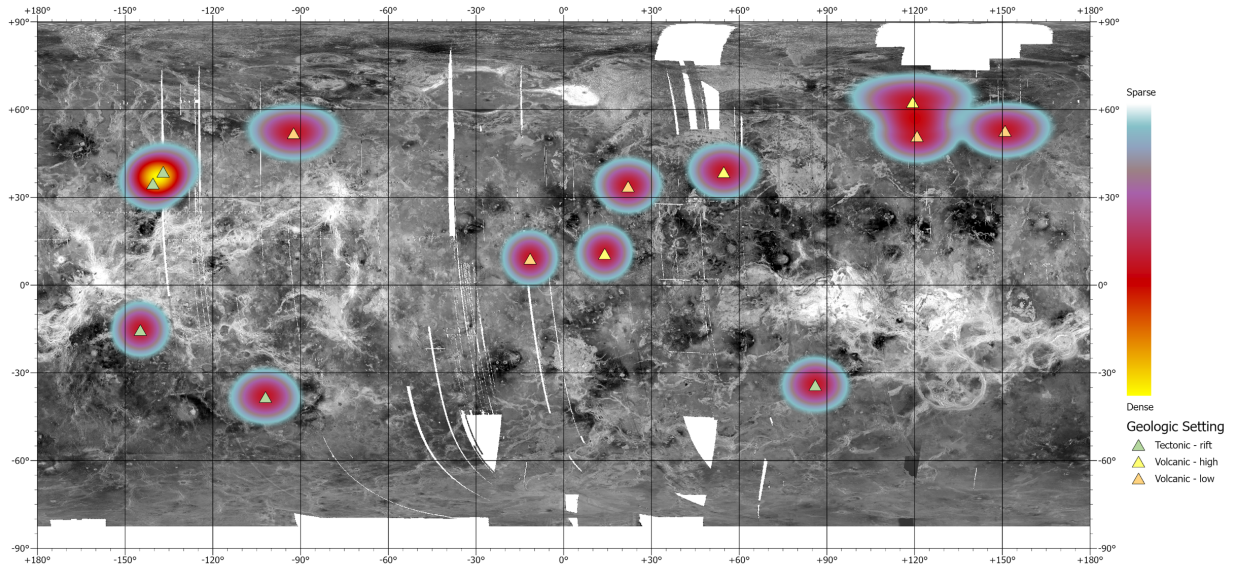

Figure 9. Heat map showing density and distribution of potential coronae on the surface of Venus. Points show exact location of features based on coordinates.

Next, two heat maps comparing the density of the official caldera and coronae populations with the distribution of the potential caldera and coronae points were created. These

maps were created to assess the accuracy of the “potential caldera” and “potential coronae” labels based on whether or not the locations of these features aligned with those of the official calderas and coronae.

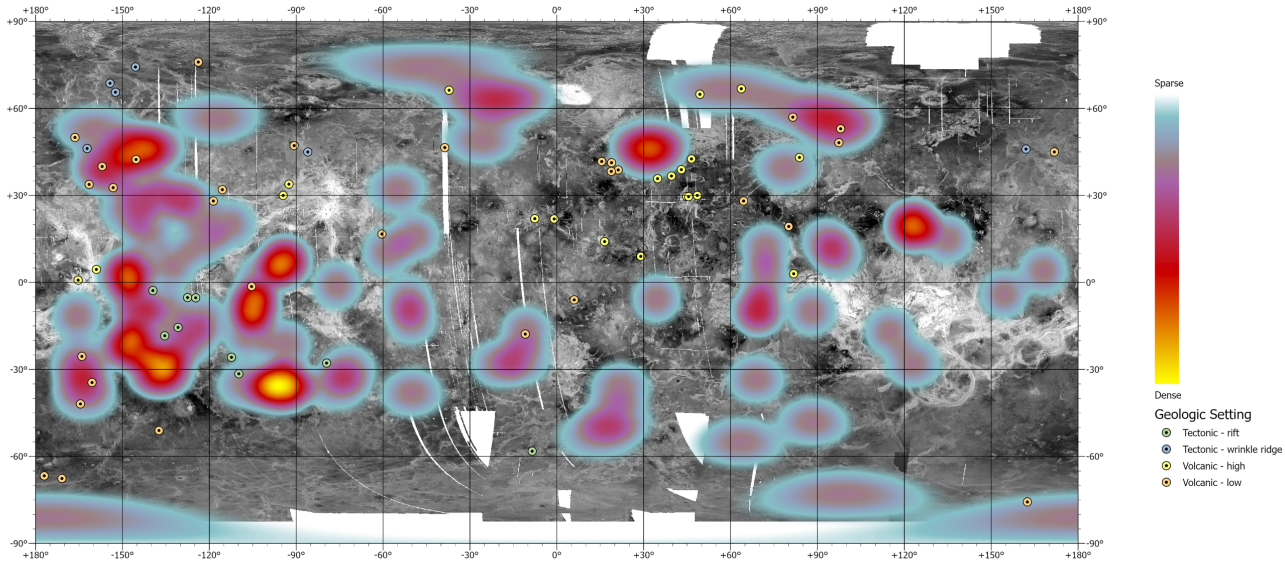

Figure 10. Heat map showing caldera density and potential caldera distribution on the surface of Venus. Points represent the potential caldera population.

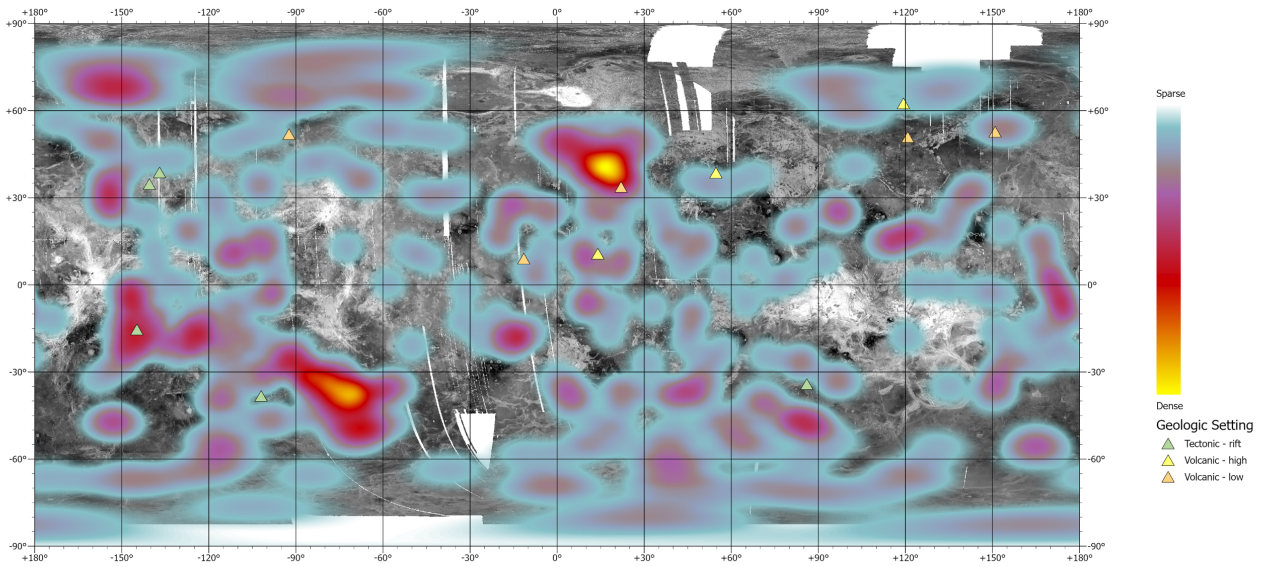

Figure 11. Heat map showing coronae density and potential coronae distribution on the surface of Venus. Points represent the potential coronae population.

Finally, a heat map with the caldera density overlaying the coronae density was made to compare distribution trends between the two populations. The purpose of this map is to identify potential “hot spots” of volcanic activity on Venus based on the density of calderas and coronae. Much overlap between caldera and coronae density can be seen throughout the surface.

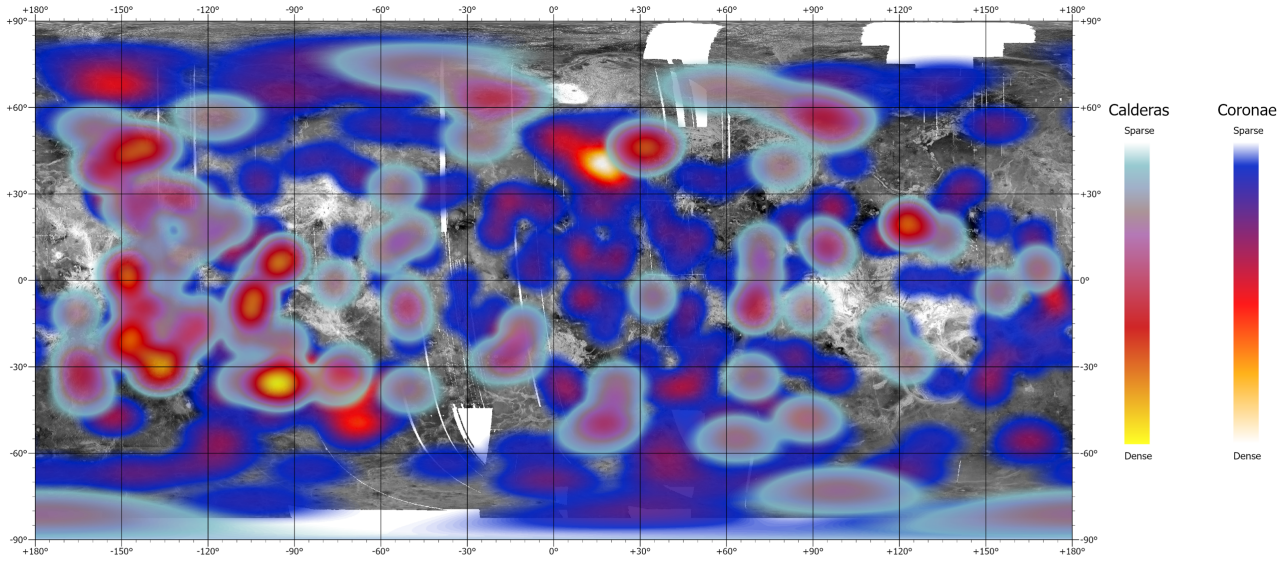

Figure 12. Heat map showing caldera density overlaying coronae density on the surface of Venus. The caldera density follows the same color scale as seen in previous maps, while the coronae density uses a darker color scale (blue to purple – lower density, red to yellow – higher density).

A more in-depth analysis of distribution trends will appear in the Discussion section.

Next, tables comparing geologic setting and feature topography for each population were created in Microsoft Excel. These tables were created to further define spatial distribution patterns of volcanic features on Venus and provide more context to the maps.

Table 3. Feature Topography vs. Geologic Setting, Calderas

	Volcanic - low	Volcanic - high	Tectonic - rift	Tectonic – wrinkle ridge	Total
dome/rise	0	0	0	0	0
rimmed rise	2	1	1	2	6
plateau	0	0	0	0	0
rimmed plateau	1	0	0	0	1
depression	12	10	14	1	37
rimmed depression	15	8	14	0	37
rim only	5	1	3	0	9
outer rim, trough, inner rise	0	0	1	0	1
no discernable signature	3	0	2	0	5
Total	38	20	35	3	96

Based on this table, the two most common feature topographies for calderas are depression and rimmed depression, and they are most likely to be found in volcanic – low and tectonic – rift settings. There are very few calderas with positive topography, which is expected because calderas are, by definition, volcanic depressions.

Table 4. Feature Topography vs. Geologic Setting, Potential Calderas

	Volcanic - low	Volcanic - high	Tectonic - rift	Tectonic – wrinkle ridge	Total
dome/rise	3	1	1	0	5
rimmed rise	1	0	1	0	2
plateau	0	2	0	0	2
rimmed plateau	2	5	1	0	8
depression	8	7	2	3	20
rimmed depression	12	5	3	3	23
rim only	3	0	0	0	3
outer rim, trough, inner rise	1	0	0	0	1
no discernable signature	1	0	1	0	2
Total	31	20	9	6	66

Again, the two most common feature topographies for potential calderas were depression and rimmed depression. Potential calderas are most commonly found in volcanic – low and volcanic – high settings. These results are consistent with the official caldera population: depression and rimmed depression are the most common feature topographies and "volcanic – low" is the most common geologic setting across both populations.

Table 5. Feature Topography vs. Geologic Setting, Coronae

	Volcanic - low	Volcanic - high	Tectonic - rift	Tectonic – wrinkle ridge	Total
dome/rise	8	5	6	0	19
rimmed rise	10	4	9	2	25
plateau	7	10	19	1	37
rimmed plateau	9	14	27	2	52
depression	19	13	5	3	40
rimmed depression	58	20	23	5	106
rim only	24	2	5	0	31
outer rim, trough, inner rise	5	5	6	1	17
no discernable signature	5	3	4	2	14
Total	145	76	104	16	341

The most common feature topography for coronae is rimmed depression. Negative topographies (depression and rimmed depression) make up ~42% of the total coronae population, while positive topographies (dome/rise, rimmed rise, plateau, rimmed plateau, and outer rim/trough/inner rise) make up 41% of the total coronae population. The majority of coronae are found in volcanic – low settings, but roughly one-third are found in tectonic – rift settings. The prevalence of coronae with negative topography is significant because one of the mechanisms behind coronae formation is volcanic uplift with only slight gravitational relaxation (Stofan et al., 1997). In theory, coronae formation should yield features with primarily positive topography.

Table 6. Feature Topography vs. Geologic Setting, Potential Coronae

	Volcanic - low	Volcanic - high	Tectonic - rift	Tectonic – wrinkle ridge	Total
dome/rise	2	0	1	0	3
rimmed rise	1	0	0	0	1
plateau	0	2	2	0	4
rimmed plateau	1	1	1	0	3
depression	0	0	0	0	0
rimmed depression	0	0	0	0	0
rim only	1	0	1	0	2
outer rim, trough, inner rise	0	0	0	0	0
no discernable signature	0	0	0	0	0
Total	5	3	5	0	13

The most common topographic profiles seen in the potential coronae population are dome/rise, plateau, and rimmed plateau. There are no potential coronae with feature topographies of depression, rimmed depression, outer rim/trough/inner rise, or no discernable signature. Potential coronae are distributed evenly across volcanic – low, volcanic – high, and tectonic – rift settings, with none found in tectonic – rift settings.

5. Discussion

5.1. Comparing Unofficial Feature Locations to Official Feature Density

For the purposes of this section, the potential caldera and coronae populations are referred to as “unofficial” features. Figures 10 and 11 show the distribution of unofficial features on the surface overlaying the respective official feature density heat maps. Figure 10 shows that, of the 66 identified potential caldera features, 28 lie within the official caldera density, 12 border the official caldera density, and 26 lie outside of the official caldera density. From these numbers, it can be determined that 40 of the potential calderas, or 61%, are either contained within or closely associated with the official caldera population. Figure 11 shows that, of the 13 identified potential coronae features, seven lie within the official coronae density, four border the official coronae density, and two lie outside of the official coronae density. From these numbers, it can be determined that 11 of the potential coronae, or 85%, are either contained within or closely associated with the official coronae population. It is significant that over half of the features in both the unofficial caldera and unofficial coronae populations are so closely associated with their official counterparts. Based on these facts, the current official caldera and coronae databases should be expanded to include these features. 41 of the 66 catalogued potential calderas are named features classified as paterae, which is a type of caldera. The USGS Gazetteer of Planetary Nomenclature identifies 73 named paterae, 32 of which are included in the official caldera population. No clear reason is given for the omission of these 41 paterae from the official caldera population, thus they should be considered as part of the official caldera population.

Additionally, class II (caldera) and class IV (elongated summit) large volcanoes as defined by Crumpler et al. (1997) should be considered as part of the official caldera population. Crumpler et al. (1997) originally excluded any calderas associated with well-defined volcanic

edifices from the official caldera population, but no concrete reason was given for this. This excludes many summit calderas, including those observed at major volcanoes on Venus like Maat Mons, Ozza Mons, and Nyx Mons. These features still qualify as calderas, regardless of their geologic setting. Class IV (elongated summit) large volcanoes often have multiple caldera-like features at their summit (Crumpler et al., 1997), so closer examination of Class IV large volcanoes would be needed to determine the presence of calderas or caldera-like features. Closer examination would also be required before adding Class IX (Corona-like interior) large volcanoes as defined by Crumpler et al. (1997) to the official coronae population in order to determine what evolutionary stage the feature is at. The close spatial associations between previously defined caldera and coronae populations, and the potential calderas and coronae identified in this catalog, warrants taking a second look at many potential calderas and coronae to determine whether or not previous populations can be expanded to include these features.

5.2. Significant Feature Concentrations

One of the regions with the highest densities of calderas and coronae on Venus is the Beta-Atla-Themis (BAT) Region, from ±180° to -30° latitude and +40° to -50° longitude (Crumpler et al., 1997). The BAT region is an area of extensive rifting and contains Hecate and Parga Chasmata, two major fracture belts. Hecate and Parga Chasmata both have associated coronae chains, extending over 8,000 km and 10,000 km, respectively (Stofan et al. 1997). There are also calderas, potential calderas, and potential coronae associated with these chains. Of the features contained in this catalog, there are nine calderas and 15 coronae within Hecate Chasmata (Table 7a). Several of these features are unnamed. In Parga Chasmata, of the features contained in this catalog, there are 18 calderas, eight potential calderas, 58 coronae, three

features included in the caldera and coronae populations, and two potential coronae (Table 8a). Again, several of these features are unnamed.

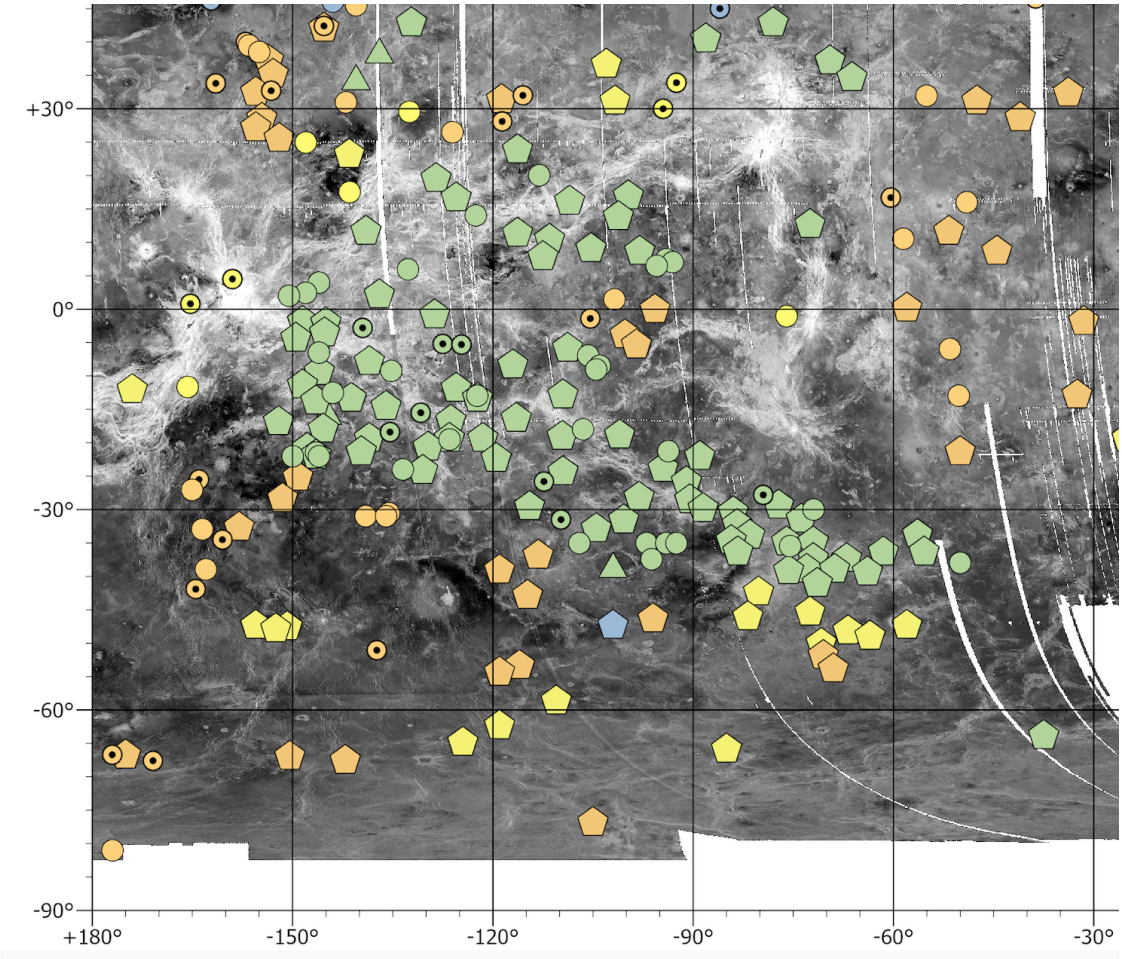

Figure 13. Beta-Atla-Themis region on Venus global map showing all catalogued features. Chasmata-associated features are denoted in green based on their "tectonic – rift" geologic setting. Calderas are represented by circles, potential calderas are represented by circles with a central point, coronae are represented by pentagons, and potential coronae are represented by triangles.

Table 7a. Hecate Chasmata Features

Feature Type	Latitude	Longitude	Dimensions (km)	Name	Feature Topography
Corona	24.2	-116.3	200	Acrea Corona	depression
Caldera	20	-113	60	Serova Patera	depression
Corona	19.9	-128.5	320	Pani Corona	plateau
Corona	17.3	-99.7	300	Sinlaku Corona	rimmed plateau
Corona	17	-125.7	500	Perchta Corona	plateau
Corona	16.5	-108.5	525	Taranga Corona	rimmed depression
Corona	14.2	-101.2	90	Nei-Teukez Corona	rimmed depression
Corona	12	-139	850	Zisa Corona	rimmed plateau
Corona	11.7	-116.3	225	Gashan-Ki Corona	no discernable signature
Corona	10.8	-111.5	375	Prthivi Corona	rimmed depression
Corona	9.4	-105.3	150	Ak-Ene Corona	rimmed plateau
Corona	9	-98	450	Aruru Corona	rimmed depression
Corona	8.2	-112.5	140	Rind Corona	rim only
Caldera	7.5	-94	90	Lama Tholus	depression
Caldera	7	-93	40	unnamed	depression
Caldera	6.5	-95.5	60	Shulzhenko Patera	depression
Caldera	6	-132.6	85	Ayrton Patera	depression
Caldera	4	-146	75	unnamed	depression
Caldera	2.5	-148	50	unnamed	depression
Corona	2.5	-137	525	Lengdin Corona	rimmed plateau
Caldera	2	-150.5	60	unnamed	depression
Caldera	1.5	-101.8	75	Garbo Patera	rim only
Corona	-5.5	-108.8	450	Javine Corona	plateau
Corona	-8	-117	200	Dhorani Corona	rimmed rise

Table 7b. Topography of Hecate Chasmata Features

dome/rise	rimmed rise	plateau	rimmed plateau	depression	rimmed depression	rim only	outer rim, trough, inner rise	no discernable signature
0	1	3	5	8	4	2	0	1

Table 8a. Parga Chasmata Features

Feature Type	Latitude	Longitude	Dimensions (km)	Name	Feature Topography
Corona	2.5	-137	525	Lengdin Corona	rimmed plateau
Corona	-0.5	-128.7	175	Blid Corona	rimmed depression
Corona	-1.5	-148.5	240	Attabeira Corona	no discernable signature
Corona	-1.7	-145	200	Chantico Corona	plateau
Potential Caldera	-2.8	-139.5	120	Rogneda Patera	rimmed depression
Corona	-3.2	-145.2	300	Pazar-ana Corona	depression
Corona	-4	-149.5	260	Tadaka Corona	rimmed rise
Potential Caldera	-5.2	-127.5	85	Cherskaya Patera	rimmed depression
Potential Caldera	-5.3	-124.7	100	Dietrich Patera	depression
Corona	-5.5	-108.8	450	Javine Corona	plateau
Caldera	-6.5	-146	100	Jotuni Patera	rimmed depression
Caldera	-7	-105.7	55	Viardot Patera	rimmed depression
Corona	-7.5	-138.5	600	Maram Corona	plateau
Corona	-8	-117	200	Dhorani Corona	rimmed rise
Caldera	-8.5	-104	50	Grechukha Tholi	rimmed depression
Corona	-9	-146	275	Ya-Yerv Corona	dome/rise
Caldera	-9	-104.5	40	Grechukha Tholi	rimmed depression
Caldera	-9.2	-135.2	100 × 140	Ledoux Patera	depression
Corona	-11	-148.5	150	Oduduwa Corona	outer rim, trough, inner rise
Corona	-11.5	-125.5	230	Lumimuut Corona	rimmed depression
Caldera	-12.5	-144	40	unnamed	depression
Corona	-12.5	-109.5	300	Ludjatako Corona	plateau
Caldera/Corona	-13	-122.3	80 × 90	Holla Corona	rimmed depression
Corona	-13	-141.2	240	Repa Corona	rimmed depression
Corona	-13.4	-146.5	210	Among Corona	rimmed depression
Corona	-14.2	-136	300	Ulgen-ekhe Coronae	rimmed depression
Potential Corona	-15.1	-144.8	400	Mbokomu Mons	rimmed plateau
Potential Caldera	-15.5	-130.8	15	Barnes Patera	rimmed depression
Corona	-16	-116.5	600	Atete Corona	outer rim, trough, inner rise
Corona	-16.3	-126.3	275	Erkir Corona	rimmed plateau
Corona	-16.5	-152.1	200	Kolias Corona	dome/rise
Corona	-17.6	-145.4	450	Rzhanitsa Corona	plateau
Caldera	-18	-106.5	60 × 100	unnamed	depression
Potential Caldera	-18.4	-135.4	60	Malibran Patera	no discernable signature
Corona	-18.5	-101	190	Nagavonyi Corona	rimmed plateau
Corona	-18.7	-109.6	220	Dilga Corona	rimmed rise
Corona	-19	-121.5	250	Aeracura Corona	rimmed plateau
Corona	-19	-126.5	350	Beruth Corona	rimmed depression
Corona	-19	-138.5	230	Onenhste Corona	depression

Caldera	-19.5	-126.5	40	unnamed	depression
Corona	-20.3	-129.7	225	Ndoi Corona	rimmed plateau
Corona	-20.5	-147.8	125	Inacho Corona	depression
Corona	-21	-139.7	260	Momu Coronae	rimmed depression
Caldera	-21.3	-93.7	75	Wilde Patera	rimmed depression
Caldera/Corona	-21.5	-146.5	225	Emegelji Coronae	rimmed depression
Corona	-21.7	-89	200	Kapenopfu Corona	dome/rise
Caldera	-22	-150	100	Villepreux-Power Patera	rimmed depression
Corona	-22	-119.5	240	Zaramama Corona	rimmed rise
Corona	-23.5	-94.5	380	Chuku Corona	plateau
Corona	-23.8	-130.5	165	Samsing Corona	no discernable signature
Caldera	-24	-133.5	75	Fedchenko Patera	rimmed rise?
Corona	-24	-109.5	460	Lalohonua Corona	rimmed plateau
Corona	-25.5	-91	250	Hervor Corona	rimmed rise
Potential Caldera	-25.8	-112.35	35	Witte Patera	rimmed rise
Corona	-27.8	-98.1	170	Kulimina Corona	plateau
Potential Caldera	-27.8	-79.5	500	Mielikki Mons	rimmed plateau
Corona	-28.2	-90.5	200	Xmukane Corona	rimmed rise
Corona	-29	-77.2	145	Anjea Corona	rimmed rise
Corona	-29.2	-114.5	330	Chanum Coronae	rim only
Corona	-29.5	-88.5	500	Lilwani Corona	rimmed plateau
Corona	-30	-84	250	Gertjon Corona	outer rim, trough, inner rise
Caldera	-30	-72	35 × 20	unnamed	no discernable signature
Corona	-31.1	-73.8	227	Durga Corona	depression
Corona	-31.2	-100.4	265	Achall Corona	rimmed rise
Potential Caldera	-31.5	-109.8	15	Destinnova Patera	dome/rise
Corona	-31.9	-83.4	300	Obiemi Corona	rimmed plateau
Corona	-32.5	-104.5	375	Oanuava Coronae	rim only
Corona	-33.4	-56.4	290	Tunehakwe Corona	rimmed plateau
Corona	-33.5	-81.5	300	Rigatona Corona	outer rim, trough, inner rise
Corona	-34.3	-84.3	91	Hutash Corona	rimmed depression
Caldera/Corona	-34.5	-76	325	Erigone Corona	outer rim, trough, inner rise
Corona	-34.5	-72	200	Santa Corona	dome/rise
Caldera	-35	-107	40	unnamed	rim only
Caldera	-35	-97	60	Zemaite Patera	no discernable signature
Caldera	-35	-94	140	Nordenflycht Patera	rimmed depression
Caldera	-35	-92.5	35	unnamed	rimmed depression
Corona	-36	-83.3	173	Parvati Corona	rimmed depression
Corona	-36	-55.4	120	Persephone Corona	rimmed depression

Corona	-36	-61.5	400	Tamiyo Corona	rimmed plateau
Corona	-37	-67	375	Semiramus Corona	rimmed plateau
Corona	-37	-72	500	Tacoma Corona	plateau
Caldera	-37.4	-96.2	60	Darclee Patera	depression
Potential Corona	-38	-102	550	unnamed	rim only
Caldera	-38	-50	100 × 60	Vovchok Patera	rimmed depression
Corona	-38.6	-73	225	Latta Corona	rimmed plateau
Corona	-38.6	-68.8	200	Zywie Corona	rimmed plateau
Corona	-38.8	-75.7	275	Shulamite Corona	plateau
Corona	-39	-63.9	300	Ukemochi Corona	rimmed plateau
Corona	-40.7	-71.4	225	Ikas Coronae	rimmed depression

Table 8b. Topography of Parga Chasmata Features

dome/rise	rimmed rise	plateau	rimmed plateau	depression	rimmed depression	rim only	outer rim, trough, inner rise	no discernable signature
5	10	9	16	9	26	4	5	5

Of the 24 catalogued features associated with Hecate Chasmata, there are 12 with explicitly negative topography: eight classified as depressions and four classified as rimmed depressions. Thus, 50% of these features, five of which are classified as coronae, have negative or depressed topography. The most common feature topography observed in the Hecate Chasmata chain is depression, which comprises roughly one-third of the catalogued features associated with Hecate Chasmata.

Of the 89 catalogued features associated with Parga Chasmata, there are 35 with explicitly negative topography: nine classified as depressions and 26 classified as rimmed depressions. There are 40 with explicitly positive topography: five classified as domes or rises, ten classified as rimmed rises, nine classified as plateaus, and 16 classified as rimmed plateaus. Thus, 39% of these features, 18 of which are coronae, have negative or depressed topography and 45% of these features, 36 of which are coronae, have positive topography. The most common feature topography observed in the Parga Chasmata chain is rimmed depression, comprising 29% of the catalogued features associated with Parga Chasmata.

It has been previously documented that coronae in trough- and rift-dominated geologic settings are more likely to have negative topography with elevated rims (Stofan et al., 1997). Thus, the prevalence of coronae with "depression" or "rimmed depression" feature topography in Hecate and Parga Chasmata is expected, but still significant because the reason behind this manifestation of coronae is unknown. Coronae have long been characterized by positive and raised topography, which is a result of the initial uplift sequence associated with their formation. However, it has been hypothesized that depressed topography could represent an additional evolutionary stage in coronae formation or indicate a lack of uplift phase (Stofan et al., 1997). While redefining and restructuring the concept of coronae on Venus is not within the scope of this thesis, the implication that not all coronae form as a result of mantle upwelling should be considered more thoroughly. Thus, higher-resolution mapping of coronae should be a priority of future research, as there are still lingering questions about their formation.

Another area with high feature densities is located between 0° and +30° latitude and +60° to +30° longitude, corresponding with the Bereghinya Planitia quadrangle (V-8), as seen in Figure 15. Bereghinya Planitia, the feature for which this quadrangle is named for, is a low volcanic plain. Figure 14 shows the high concentration of features seen in this region, consisting of 23 coronae and one potential corona present in the catalog of named features. There are multiple major ridge belts present in the V-8 quadrangle, as well as

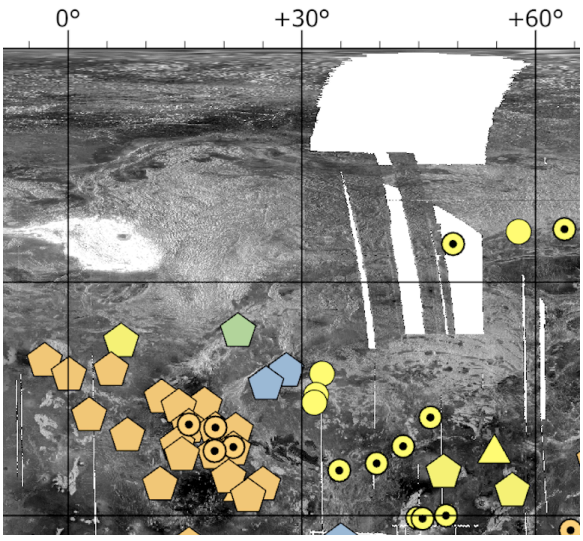

Figure 14. Bereghinya Planitia cluster on Venus global map showing all catalogued features. All features associated with this cluster are denoted in orange to reflect their "volcanic – low" geologic setting, other than Damona and Edda Coronae, which are denoted in blue to reflect their "tectonic – wrinkle ridge" geologic setting.

many smaller wrinkle ridges and areas of deformation that link the coronae together, forming a chain (McGill, 2004). Two features, Damona and Edda Coronae, are more closely associated with the Ausra Dorsa ridge belt but have been included in the Bereghinya Planitia feature cluster due to their proximity. Additionally, four of the Bereghinya Planitia coronae, Sand; Trotula; Yaroslavna; and Cavell, were previously categorized as paterae according to the USGS Gazetteer of Planetary Nomenclature.

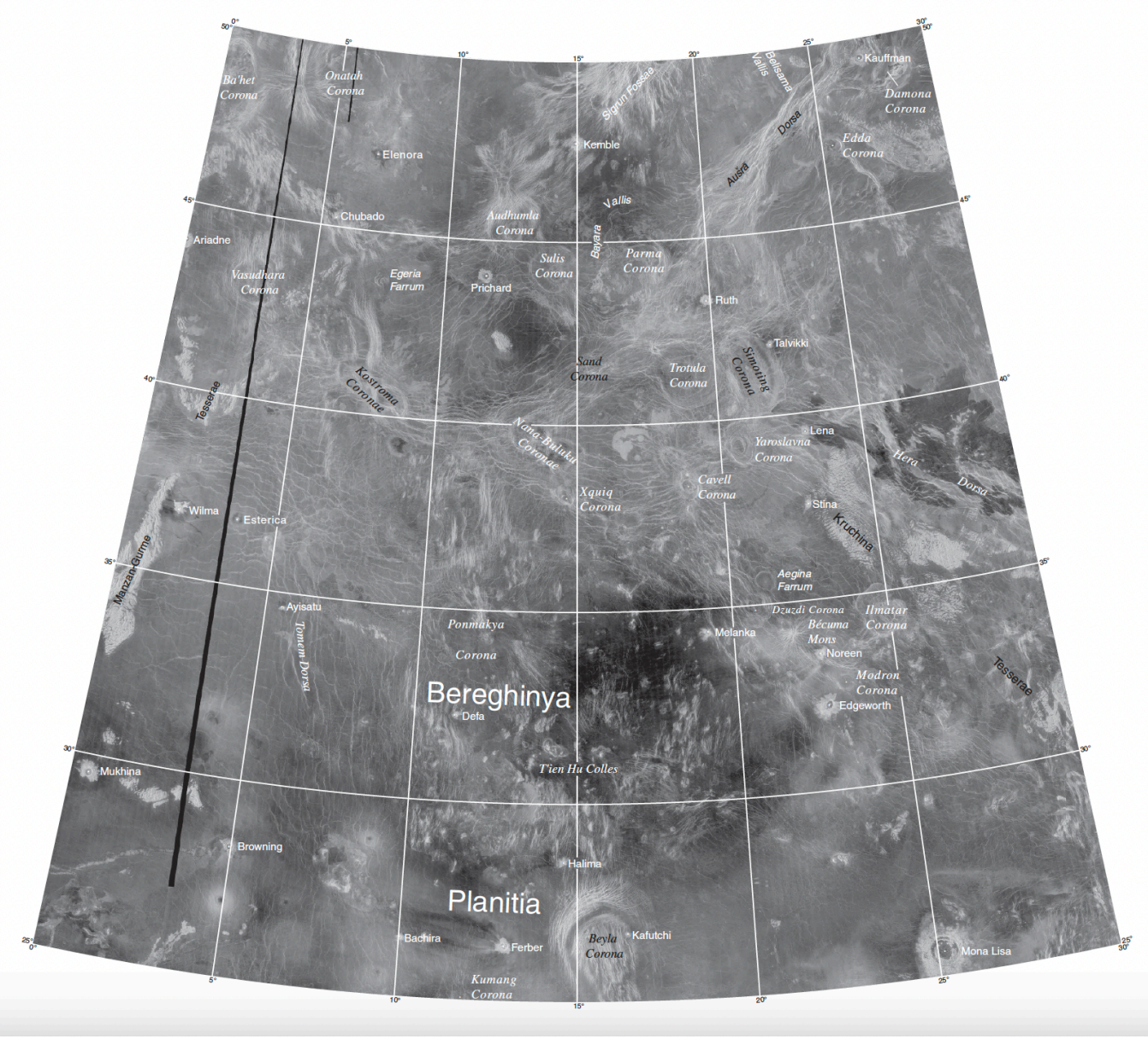

Figure 15. Radar map of the Bereghinya Planitia Quadrangle (V-8) on Venus. Map scale 1:5,000,000.

Table 9a. Bereghinya Planitia Features

Feature Type	Latitude	Longitude	Dimensions (km)	Name	Feature Topography
Corona	49	5.5	298	Onatah Corona	rimmed plateau
Corona	48.9	28	140	Damona Corona	rimmed depression
Corona	48.4	0.1	145	Ba'het Corona	rimmed depression
Corona	47.2	25.4	50	Edda Corona	rimmed depression
Corona	45.5	12	225	Audhumla Corona	rimmed depression
Corona	44.5	17.5	110	Parma Corona	rimmed depression
Corona	44.3	14.2	136	Sulis Corona	rimmed depression
Corona	43.2	2.7	160	Vasudhara Corona	depression
Potential Caldera/Corona	41.7	15.5	181	Sand Corona	rimmed depression
Potential Caldera/Corona	41.3	18.9	146	Trotula Corona	rimmed depression
Corona	41.2	21.5	270	Simoting Corona	rimmed depression
Corona	40.6	7.6	230	Kostroma Coronae	rimmed depression
Corona	39.4	14	230	Nana-Buluku Coronae	rimmed depression
Potential Caldera/Corona	38.8	21.2	112	Yaroslavna Corona	rimmed depression
Potential Caldera/Corona	38.3	18.8	100	Cavell Corona	depression
Corona	38.1	14.6	55	Xquiq Corona	rimmed depression
Corona	35.2	20.6	80	Dzuzdi Corona	rimmed depression
Corona	34.3	25	110	Ilmatar Corona	rimmed depression
Corona	34.3	11.8	280	Ponmakya Corona	rimmed depression
Potential Corona	34	22	200	Becuma Mons	dome/rise
Corona	32.8	23.1	50	Modron Corona	depression
Corona	26.5	15.5	400	Beyla Corona	outer rim, trough, inner rise
Corona	25	11.8	40	Kumang Corona	dome/rise
Corona	23.3	21.6	180	Asomama Corona	rimmed depression

Table 9b. Topography of Bereghinya Planitia Features

dome/rise	rimmed rise	plateau	rimmed plateau	depression	rimmed depression	rim only	outer rim, trough, inner rise	no discernable signature
2	0	0	1	3	17	0	1	0

Of the 24 catalogued features associated with Bereghinya Planitia there are 20 with explicitly negative topography, three classified as depressions and 17 classified as rimmed depressions. 83% of the features associated with Bereghinya Planitia, all of which are coronae,

have negative or depressed topography. Rimmed depression is also the most common feature topography observed in the Bereghinya Planitia cluster.

The coronae cluster in Bereghinya Planitia, which has not been previously documented, is considered significant for multiple reasons. First, this feature cluster occurs outside the BAT region, which has the highest concentration of coronae, calderas, and other volcanic features on the surface of Venus. One common trait shared by the coronae cluster associated with Bereghinya Planitia and the coronae chains of Hecate and Parga Chasmata is highly deformed terrain. The Bereghinya Planitia quadrangle has multiple ridge belts and smaller wrinkle ridges linking the coronae, while the Hecate and Parga Chasmata coronae chains lie along fracture belts. This may indicate a relationship between highly deformed terrain and the formation of feature clusters on Venus. The emplacement of ridge belts and coronae occurred at the same time, during the global tectonic regime during the Fortunian to mid-Guineverian periods of the stratigraphic history of Venus. (Ivanov & Head, 2015). Wrinkle ridges would have occurred after this time during the global volcanic regime of the mid-Guineverian period. The Bereghinya Planitia quadrangle is dominated by multiple ridge belts, so it is incredibly likely that the coronae cluster formed around the same time as the ridge belts, with wrinkle ridges being emplaced afterwards. Thus, the formation of ridge belts created an environment in Bereghinya Planitia that was more conducive to coronae formation.

Another reason for this significance is that it occurs outside of the three distinct geologic environments common for coronae as identified by Stofan et al. (1997): volcanic rises, chasmata, and isolated in volcanic plains. While Bereghinya Planitia is a volcanic plain, its associated features are not isolated and form a chain similar to those seen at Hecate and Parga Chasmata. Additionally, the coronae at Bereghinya Planitia were originally described as “arachnoids” by

members of the Soviet *Venera* 15 and 16 teams (Barsukov et al., 1986). The coronae are connected by extensive, closely spaced wrinkle ridges, which create a spider-like appearance, hence the "arachnoid" classification. However, the use of the term "arachnoid" has been largely discontinued in recent years because it ignores the similarities between the coronae cluster in the Bereghinya Planitia quadrangle to coronae elsewhere on Venus. (McGill, 2004). Thus, other clusters previously classified as "arachnoids" should be re-examined to see whether or not they exhibit features similar to known coronae clusters and chains.

The most recent data from Venus is over 30 years old. Upcoming missions will enable further analysis of calderas and coronae on Venus by providing more precise, higher-resolution radar maps of the surface. With these updated maps, one of the main research priorities should be taking a look at the caldera and coronae populations of Venus for the purpose of identifying more significant coronae clusters, assessing the validity of the potential caldera and coronae populations and whether or not they fit in with previously observed feature populations, and further characterization of coronae with depressed topography.

6. Conclusion

The original purpose of this thesis was to build on previous schema used to characterize volcanic features on the surface of Venus with a specific focus on coronae and calderas, as well as caldera-like and coronae-like features, and to construct a global map of coronae and calderas to investigate their spatial relationship. Through the identification of potential caldera-like and coronae-like features and comparing their distribution to the density and distribution of "official" calderas and coronae on the surface of Venus, it was found that over half of these features are in close proximity to previously observed calderas and coronae. When analyzing the overall density of calderas and coronae on Venus, a previously undocumented coronae cluster was identified within the Bereghinya Planitia quadrangle. This cluster occurs outside of the typical geologic settings for coronae on Venus, but the surrounding terrain is highly deformed from wrinkle ridges and larger ridge belts. This, along with the prevalence of coronae chains in the BAT region, another area of high deformation due to extensive fracture and rift belts, suggests that the presence of deformed terrain may contribute to the formation of feature clusters on the surface of Venus. It was found that the formation of ridge belts in Bereghinya Planitia was likely more conducive to coronae formation because these features were emplaced during the same period in the stratigraphic history of Venus. Additionally, it introduces the need to re-examine other feature clusters on Venus that may be characterized as "arachnoids", an ultra-specific, outdated term that is no longer used to describe coronae clusters linked by extensive wrinkle ridges.

Despite the discoveries of previous missions to Venus, including the influential radar mapping conducted by *Magellan*, there is still much to be discovered about Earth's evil twin. The lingering questions remaining from this thesis include the prevalence of coronae with depressed topography, and whether or not this can be explained by their formation and evolution.

Upcoming missions to Venus will provide higher-resolution maps of the surface, which will allow researchers to observe these features in a more in-depth way than was previously possible. While it is outside of the scope of this thesis to unilaterally redefine the schematics used to characterize volcanic features on Venus, the hope is that this research can be continued in order to learn more about the formation, evolution, classification, and spatial distribution of calderas and coronae.

References

Barsukov, V. L., Basilevsky, A. T., Burba, G. A., et al. (1986). The geology and geomorphology of the Venus surface as revealed by the radar images obtained by *Venera* 15 and 16. *Journal of Geophysical Research: Solid Earth*, 91(B4), pp. 378-398. https://doi.org/10.1029/JB091iB04p0D378

Basilevsky, A. T. & Head, J. W. (1995). Global stratigraphy of Venus: analysis of a random sample of thirty-six test areas. *Earth, Moon, and Planets*, 66(3), pp. 285-336. https://doi.org/10.1007/BF00579467

Basilevsky, A. T. & Head, J. W. (1995). Regional and global stratigraphy of Venus: a preliminary assessment and implications for the geological history of Venus. *Planetary and Space Science*, 43(12), pp. 1523-1553. https://doi.org/10.1016/0032-0633(95)00070-4

Basilevsky, A. T., Head, J. W., Schaber, G. G., & Strom, R. G. (1997). The resurfacing history of Venus. In S. W. Bougher, D. Hunten, & R. Phillips, Venus II - geology, geophysics, atmosphere, and solar wind environment (pp. 1047-1084). Tuscon: The University of Arizona Press.

Basilevsky, A. T. & Head, J. W. (1998). The geologic history of Venus: A stratigraphic view. *Journal of Geophysical Research: Planets*, 103(E4), pp. 8531-8544. https://doi.org/10.1029/98JE00487

Campbell, B. A. & Rogers, P. G. (1994). Bell Regio, Venus: Integration of remote sensing data and terrestrial analogs for geologic analysis. *Journal of Geophysical Research: Planets*, 99(E10), pp. 21153-21171. https://doi.org/10.1029/94JE01862

Cattermole, P. (1994). Venus, the Geological Story. Baltimore: The Johns Hopkins University Press.

Crumpler, L. S., Aubele, J. C., Senske, D. E. et al. (1997). Volcanoes and centers of volcanism on Venus. In S. W. Bougher, D. Hunten, & R. Phillips, Venus II - geology, geophysics, atmosphere, and solar wind environment (pp 697-756). Tucson: The University of Arizona Press.

Ford, J. P. (1993). *Magellan*: the mission and the system. In J. P. Ford, J. J. Plaut, C. M. Weitz, et al., Guide to *Magellan* Interpretation. JPL Publication 93-24.

Ford, J. P. & Plaut, J. J. (1993). *Magellan* image data. In J. P. Ford, J. J. Plaut, C. M. Weitz, et al., Guide to *Magellan* Interpretation. JPL Publication 93-24.

Guest, J. E. & Stofan, E. R. (1999). A new view of the stratigraphic history of Venus. *Icarus*, 139(1), pp. 55-66. https://doi.org/10.1006/icar.1999.6091

Hahn, R. M. & Byrne, P. K. (2023). A morphological and spatial analysis of volcanoes on Venus. *Journal of Geophysical Research: Planets*, 128(4). https://doi.org/10.1029/2023JE007753

Hamilton, V. E. & Stofan, E. R. (1996). The geomorphology and evolution of Hecate Chasma, Venus. *Icarus*, 121(1), pp. 171-194. https://doi.org/10.1006/icar.1996.0077

Hansen, V. L., Willis, J. J., & Banerdt, W. (1997). Tectonic overview and synthesis. In S. W. Bougher, D. Hunten, & R. Phillips, Venus II - geology, geophysics, atmosphere, and solar wind environment (pp. 797-844). Tucson: The University of Arizona Press.

Head, J. W., Crumpler, L. S., & Aubele, J. C. (1992). Venus volcanism: classification of volcanic features and structures, associations, and global distributions from *Magellan* data. *Journal of Geophysical Research: Planets*, 97(E8), pp. 13153-13197. https://doi.org/10.1029/92JE01273

Herrick, R. R., Stahlke, D. L., & Sharpton, V. L. (2012). Fine-scale Venusian topography from *Magellan* stereo data. *Eos, Transactions American Geophysical Union*, 93(12), pp. 125-126. https://doi.org/10.1029/2012EO120002

Herrick, R. R., & Hensley, S. (2023). Surface changes observed on a Venusian volcano during the *Magellan* mission. *Science*, 379(6638), pp. 1205-1208. https://doi.org/10.1126/science.abm7735

Hunt, G. E., & Moore, P. (1982). The Planet Venus. London: Faber and Faber Limited.

Ivanov, M. A. & Head, J. W. (2015). The history of tectonism on Venus: A stratigraphic analysis. *Planetary and Space Science*, 113-114, pp. 10-32. https://doi.org/10.1016/j.pss.2015.03.016

Lyons, D. T., Saunders, R. S., & Griffith, D. G. (1995). The *Magellan* Venus mapping mission: aerobraking operations. *Acta Astronautica*, 35(9-11), pp. 669-676. https://doi.org/10.1016/0094-5765(95)00032-U

Martin, P., Stofan, E. R., Glaze, L. S., & Smrekar, S. E. (2007). Coronae of Parga Chasma, Venus. *Journal of Geophysical Research: Planets*, 112(E4). https://doi.org/10.1029/2006JE002758

McGill, G. E. (2004). Geologic map of the Bereghinya Planitia quadrangle (V-8), Venus. U.S. Geological Survey Geologic Investigations Series I-2794. https://pubs.usgs.gov/imap/i2794/

Mouginis-Mark, P. J. (2016). Geomorphology and volcanology of Maat Mons, Venus. *Icarus*, 277, pp. 433-441. https://doi.org/10.1016/j.icarus.2016.05.022

Phillips, R. J., Raubertas, R. F., Arvidson, R. E., et al. (1992). Impact craters and Venus resurfacing history. *Journal of Geophysical Research: Planets*, 97(E10), pp. 15923-15948. https://doi.org/10.1029/92JE01696

Saunders, R. S., Spear, A. J., Allin, P. C., et al. (1992). Magellan mission summary. *Journal of Geophysical Research: Planets*, 97(E8), pp. 13067-13090. https://doi.org/10.1029/92JE01397

Schaber, G. G., Strom, R. G., Moore, H. J., et al. (1992). Geology and distribution of impact craters on Venus: What are they telling us? *Journal of Geophysical Research: Planets*, 97(E8), pp. 13257-13301. https://doi.org/10.1029/92JE01246

Sheehan, W. & Limaye, S. S. (2022). Venus. London: Reaktion Books Ltd.

Siddiqi, A. A. (2018). Beyond Earth: a chronicle of deep space exploration, 1958-2016. Washington, D. C.: National Aeronautics and Space Administration, Office of Communications, NASA History Division.

Stofan, E. R, Sharpton, V. L., Schubert, G., et al. (1992). Global distribution and characteristics of coronae and related features on Venus: implications for origin and relation to mantle processes. *Journal of Geophysical Research: Planets*, 97(E8), pp. 13347-13378. https://doi.org/10.1029/92JE01314

Stofan, E. R., Hamilton, V. E., Janes, D. M., & Smrekar, S. E. (1997). Coronae on Venus: morphology and origin. In S. W. Bougher, D. Hunten, & R. Phillips, Venus II - geology, geophysics, atmosphere, and solar wind environment (pp 931-965). Tucson: The University of Arizona Press.

Stofan, E. R., Smrekar, S. E., Mueller, N., & Helbert, J. (2016). Themis Regio, Venus: Evidence for recent (?) volcanism from VIRTIS data. *Icarus*, 271, pp. 375-386. https://doi.org/10.1016/j.icarus.2016.01.034

Strom, R. G., Schaber, G. G., & Dawson, D. D. (1994). The global resurfacing of Venus. *Journal of Geophysical Research: Planets*, 99(E5), pp. 10899-10926. https://doi.org/10.1029/94JE00388

Tanaka, K. L., Schaber, G. G., Chapman, M. G., et al. (1993). The Venus geologic mappers' handbook. U.S. Geological Survey Open-File Report 93-516. https://doi.org/10.3133/ofr93516

Widemann, T., Smrekar, S.E., Garvin, J.B., et al. (2023). Venus Evolution Through Time: Key Science Questions, Selected Mission Concepts and Future Investigations. *Space Science Reviews*, 219(56). https://doi.org/10.1007/s11214-023-00992-w

Young, C. (1990). The *Magellan* Venus explorer's guide. JPL Publication 90-24.